EFFECT OF CONTINUOUS WAVE LASER IRRADIATION ON STRUCTURAL RELAXATION AND MECHANICAL PROPERTIES OF FE-SI-B AMORPHOUS RIBBON

By

MD FARHADUL HAQUE

Bachelor of Science in Mechanical Engineering

Bangladesh University of Engineering and Technology

Dhaka, Bangladesh

2009

Submitted to the Faculty of the
Graduate College of the
Oklahoma State University
in partial fulfillment of
the requirements for
the Degree of
MASTER OF SCIENCE
December, 2013

EFFECT OF CONTINUOUS WAVE LASER

IRRADIATION ON STRUCTURAL RELAXATION

AND MECHANICAL PROPERTIES OF FE-SI-B

AMORPHOUS RIBBON

Thesis Approved:

Dr. Sandip P. Harimkar

Thesis Adviser

Dr. Ali Kaan Kalkan

Dr. Matthew J. Klopfstein

ACKNOWLEDGEMENTS

I would like to acknowledge the financial support from the National Science Foundation (CMMI 0969255) for this project. I would also like to thank Dr. Narendra Dahotre, Hitesh Vora, and Shravana Katakam from University of North Texas for their support during experiments. Finally, I am grateful to my family for their continuous support throughout my thesis.

Name: Md Farhadul Haque

Date of Degree: DECEMBER, 2013

Title of Study: EFFECT OF CONTINUOUS WAVE LASER IRRADIATION ON STRUCTURAL RELAXATION AND MECHANICAL PROPERTIES OF FE-SI-B AMORPHOUS RIBBON

Major Field: Mechanical Engineering

Abstract: The thermal treatment of amorphous alloys results in change in their properties due to structural relaxation and crystallization. Laser irradiation permits very high control in site-specific thermal treatment of material. The present study was aimed at investigating structural relaxation and resulting change in mechanical properties of Fe-Si-B amorphous ribbon under laser irradiation. The alloy was irradiated by a continuous wave Nd:YAG laser. Three different scanning speeds (500, 600, and 700 mm/s) were chosen with constant laser power at 100 W. No crystallization was observed from microstructural and XRD analyses. Thermal simulation revealed that the maximum temperature was 357 °C, which was below crystallization temperature of the alloy. DSC analysis revealed structural relaxation for all the scanning speeds. Thermal embrittlement, microhardness and structural distortion were measured and related with relaxation and laser scanning speed. Reduction in fracture stress and strain were more than 50% for 500 mm/s. Microhardness was increased by 4-5%. Structural distortion was enhanced at lower laser scanning speed. Thermal stress was found to be tensile in nature at the middle of the irradiated area and as high as 350 MPa. Since there was no other than thermal load acting on the material during irradiation, it seems that the thermal stress was responsible for the structural distortion.

TABLE OF CONTENTS

LIST OF TABLES

LIST OF FIGURES

CHAPTER 1

INTRODUCTION

1.1. Amorphous alloy

Over the last 5 decades, amorphous alloys have been a topic of great interest, mainly due to their improved properties compared to conventional alloys. Amorphous alloys possess better tensile strength, corrosion resistance, wear resistance and hardness than crystalline alloys [1-4]. Absence of grain boundaries is the main characteristic of the amorphous alloy, which distinguishes it from its crystalline counterparts. In a conventional casting method, liquid melt starts to solidify with the presence of nuclei or external surfaces such as mold wall [5]. Each nucleus starts to solidify as a single crystal. When two such single crystals meet each other with sufficient misorientation, grain boundary is formed. These grain boundaries are known as line defects in the microstructure. Grain boundaries are avoided in amorphous alloys by rapid solidification. In this process, the liquid melt is solidified at a cooling rate fast enough to retain the same random molecular structure it has in liquid form. Therefore, disordered atomic structure is the unique feature of amorphous alloys which makes it an attractive metallic system for many applications where hardness, strength, corrosion resistance, magnetic property and even aesthetic property [6-13] are concerned.

1.2. Glass forming ability

Formation of glass forming ability is dictated by the following parameters [14-16]:

1. Critical cooling rate
2. Number of components in the alloy system
3. Atomic size difference among the components
4. Temperature difference between Glass transition and Crystallization

Klement *et al* first introduced a solidification process fast enough to prevent the formation of crystals [17]. In their experiment, amorphous structure was formed by injecting a droplet of liquid melt in to a liquid quenching bath. But this process restricted the size of the alloy. In addition, critical cooling rate is a dominant factor in preparing amorphous alloy, which was very high in this process. The cooling rate was in the order of 10^6 K/s. It is difficult to maintain this rate in a practical scenario where bulk production is one of the key concerns. Introducing multicomponent alloy systems can reduce the critical cooling rate required to retain amorphous structure.

Glass forming ability is obtained in the condition of low free energy for the transformation of liquid to its crystalline phase [15]. Free energy (ΔG) is given by the equation $\Delta G = \Delta H_f - T\Delta S_f$ where ΔH_f, T and ΔS_f are defined as enthalpy of fusion, temperature, and entropy of fusion respectively. Low ΔG occurs when ΔH_f is low and large ΔS_f. ΔS_f is proportional to the number of microscopic states. So, large ΔS_f is expected in multicomponent systems. ΔHf decreases with the increase in the degree of dense random packing, which is favorable in multicomponent systems. So, multicomponent systems containing more than three elements favor the formation of amorphous structure. Critical cooling rate tends to decrease with increase in ΔT_x [18, 19]. ΔT_x is defined as the difference between glass transition temperature and

crystallization temperature. Difference in atomic size among the components in an alloy also facilitates glass formation. Atomic size ratio of about 10% among the components results in dense packing structure and large liquid/solid interfacial energy, which are essential for amorphous structure formation [15].

1.3. Stability of glassy structure

Metallic glasses have metastable structure [20]. Due to vitrification, amorphous structure has slightly lesser density than its crystalline state of a particular alloy system. As a result, interatomic distance in an amorphous structure is slightly larger, resulting in free volume which allows the atoms to rearrange among themselves under the influence of external force such as thermal annealing. It leads towards the equilibrium state through crystal formation. If the annealing temperature stays below crystallization temperature, the atomic movement is not sufficient enough to form crystals, but leads toward short range ordering. This phenomenon is known as structural relaxation. These may cause changes in their physical, mechanical, and chemical properties [21-24]. In some cases, it causes undesired change in their properties, such as embrittlement [25, 26], which restricts their application. But careful thermal treatment can change the properties to a desired level. Poor ductility has been a limitation to amorphous structure, and often causes catastrophic failure. Plastic flow in amorphous structure is localized into shear bands [27-29]. Introducing nano precipitates into amorphous structure facilitate plastic flow, hence improving ductility. Some previous works [30-32] showed that ferromagnetic metallic glasses exhibit excellent soft magnetic properties in structurally relaxed and partially crystallized states. These make thermal treatment of amorphous structure a topic of great interest in present days.

1.4. Laser for thermal treatment of amorphous alloys

Laser is the abbreviation of Light Amplification by Stimulated Emission of Radiation. It is a coherent, convergent and monochromatic beam of electromagnetic radiation with wavelengths

ranging from ultraviolet to infrared. Because of the directional nature of the laser beam, it can be focused on a very small area, even at longer distances. Highly directional beams are known as highly collimated beams. The degree of collimation is directly related with the beam divergence angles [33]. Lasers have a wide area of application in the fields of engineering, medicine, and electronics [34-37]. Lasers are generally classified into four types based on the physical nature of the active medium used: solid-state lasers, gas lasers, semiconductor lasers, and dye lasers. Based on the output of the laser, it can be classified as continuous or periodic. In continuous beam operation, constant laser energy is discharged. In pulsed mode of operation, the energy is applied for a specific time and then switched off.

Thermal treatment of amorphous structure is carried out through furnace heating. Griner *et al* showed that the structure and properties of $Fe_{78}Si_9B_{13}$ amorphous ribbon changed through the relaxation process achieved by furnace heating [20]. They reported change in tensile strength for relaxed ribbon, which increased initially but later decreased due to short range ordering of atoms. One of the major disadvantages of furnace heating is that the location of crystal formation cannot be controlled, which can be overcome if laser processing is introduced. It has been a popular method for thermal treatment of alloys for its non-contact process and superior control over process parameter for precise and concentrated heating [38-40]. Rapid cooling rate is another advantage of laser which makes it ideal for processing and surface coating of amorphous structure [41]. Laser power and scanning speed are the two key process parameters in material processing with continuous type laser, whereas pulse energy and pulse frequency are the two key parameters for pulsed laser system.

CHAPTER 2

LITERATURE REVIEW

2.1. Laser processing of amorphous material

A number of researches have been conducted to report the laser induced crystallization and relaxation of amorphous structure. In some works, initiation of defects was reported as a result of laser irradiation. Sinke [42] *et al* reported enhancement of relaxation of a-Si under the influence of pulsed-laser irradiation. In their experiment, laser energy density was kept just below the threshold of surface melting of the material (0.1 J/cm^2) with varying number of pulses (pulse length was 32 ns). Relaxation was revealed through Raman spectroscopy where shift in the Transverse Optic (TO) was observed towards higher wave numbers. Formation of high density electron-hole pairs was reported during laser irradiation, which ultimately softened the amorphous silicon network and enhanced relaxation. Bond angle distortion in the silicon network was found to decrease with increase in the number of pulses during laser irradiation. Although temperature rise during laser irradiation was higher than crystallization temperature, no crystal formation was detected from Raman spectroscopy. They stated this was due to low nucleation rate and growth, unable to form substantial amount of crystallite to get detected. Lanotte [43] reported relation between continuous wave laser irradiation and

magnetostriction for Fe-based amorphous alloy for 0.5 s irradiation time and three different laser powers as 20 W, 40 W and 80 W. Irradiation induced temperature was lower than crystallization temperature. Comparing with untreated ribbon, a decrease in permeability was observed under tensile force. It was reported that irradiated areas required lesser activation energy because of atomic rearrangement. He also reported that irradiation was the reason for local defects and stress sites which was activated under tensile load and finally inhibited initial magnetization. Mudry and Nykyruy reported structural change of Fe-based amorphous ribbon irradiated by pulsed laser [44]. In their experiment, pulse energy was varied from 0.134 mJ to 0.245 mJ with pulse duration of 130 ns and pulse frequency of 50 Hz. They reported gradual structural change with change in the pulse energy, revealed from XRD analysis. It was reported that at lower energy (below 0.245 mJ), nucleation and atomic clusters were formed. But both energy and time was not sufficient enough for the clusters to arrange into fully defined crystals, ultimately resulted in short range ordering.

2.2. Laser processing of $Fe_{85\text{-}95\%}Si_{5\text{-}10\%}B_{1\text{-}5\%}$ amorphous alloy

$Fe_{85\text{-}95\%}Si_{5\text{-}10\%}B_{1\text{-}5\%}$ is a popular metallic glass system used in transformers and motors for its extremely low core loss. Dahotre [45-47] *et al.* conducted a number of experiments where laser induced nano crystallization was reported for this system. In all of their works, formation of nano-crystals was detected by crystallographic peak observed in the XRD analyses. In one study, minimum laser energy for crystallization was reported as 0.17 J/mm^2, where sample thickness was 40 μm. Pulsed laser system was used in that experiment with pulse width and pulse repetition rate of about 0.5 ms and 20 Hz respectively. Thermal embrittlement was reported as a result of crystallization (for higher laser energy) and structural relaxation (in case of lower laser energy). In another work, where continuous wave laser was used, minimum laser energy for crystallization was reported as 0.33 J/mm^2, where sample thickness was 28 μm. Variation in microstructure was observed across the laser track. Crystallization in the middle was suppressed by high cooling rate, although the temperature in the middle was higher than crystallization temperature during laser

irradiation. Even though the edge of the track experienced temperature below crystallization temperature, crystal formation was observed from TEM image analysis. This crystal formation was reported as a result of thermally induced compressive stress. Shear band was found in the compressive region from microstructural analysis. Since shear bands contain homogeneously distributed free volume and transformation from amorphous to crystalline phase is diffusion controlled, it was believed that stress induced shear band enhanced diffusion for nano-crystal formation at the edge of the track.

CHAPTER 3

SCOPE AND OBJECTIVES

Most of the works on $Fe_{85\text{-}95\%}Si_{5\text{-}10\%}B_{1\text{-}5\%}$ amorphous alloy focused on laser induced crystallization and its characterization. Little emphasis had been put on laser induced structural relaxation for this type of alloy system so far. Therefore, present study is aimed at laser induced structural relaxation on $Fe_{85\text{-}95\%}Si_{5\text{-}10\%}B_{1\text{-}5\%}$ amorphous alloy and corresponding change in its mechanical properties. The mentioned alloy was irradiated by continuous wave laser at constant laser power with varying laser scanning speeds. Structural relaxation was revealed in Differential Scanning Calorimetry (DSC) analysis and correlated with laser scanning speed. Tensile strength, microhardness and surface deformation of the irradiated alloys were measured and correlated with laser processing parameters and structural relaxation as well. A heat transfer model capable of getting temperature profile due to irradiation was developed to assist the experimental observations.

CHAPTER 4

MATERIALS AND METHODS

4.1. Experimental Details

4.1.1. Laser processing

Iron-based amorphous ribbons of composition of $Fe_{85-95}Si_{5-10}B_{1-5}$ (at. %) with thickness of about 22 μm and width of about 25 mm (Supplier: Metglas Inc.; Product No.: 2605 SA1) were used in this investigation for laser surface irradiation. The ribbons were cut into tensile test specimens as per ASTM E394-93 standard (Gage length of 2 inch). Emery paper of 240 grit size was used as the grip section of the specimen. One surface of these tensile samples was then irradiated with an IPG YLS-3000 fiber laser operated with 1.064 μm wavelength in continuous wave (CW) mode. The laser beam had a TEM_{00} energy profile (Gaussian distribution). The laser was scanned with three different laser scanning speeds, 500, 600 and 700 mm/s at a laser power of 100 W. The laser spot diameter was maintained at 0.6 mm. The distance between two parallel laser tracks was maintained at 3 mm. A schematic of the laser processing is shown in Fig. 1.

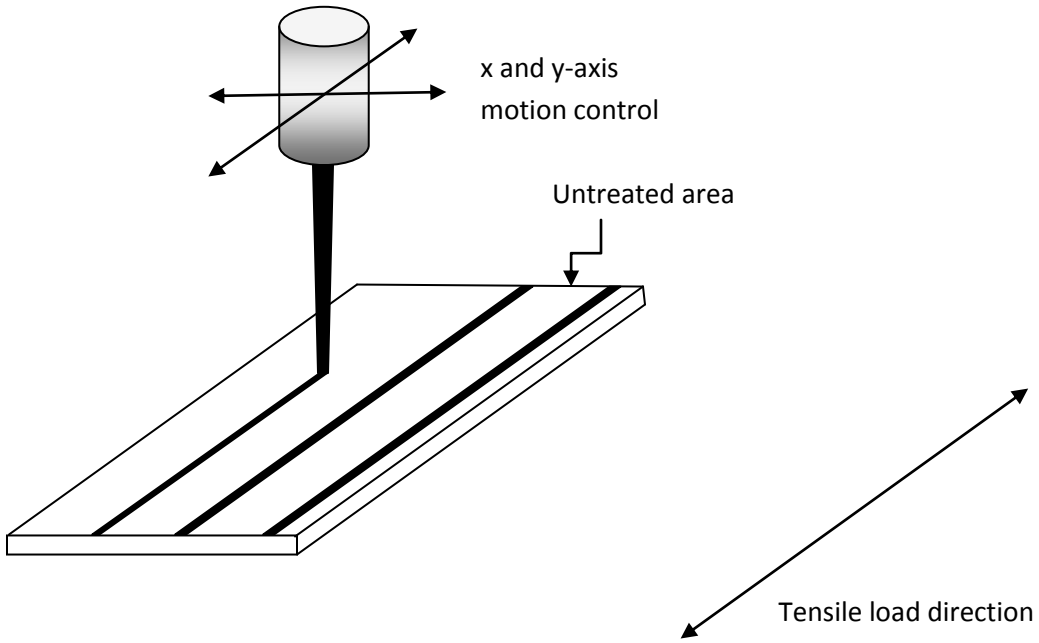

Figure 1: Schematic of laser processing

4.1.2. Tensile test and microstructural analysis

After laser irradiation, the samples were tested for tensile properties at room temperature (Make: Instron; Model: 5582, illustrated in Fig. 2). The extension rate was maintained at 0.1 in/min for all cases. Slippage between grip section and the samples occurred in some cases during tensile tests. The data for unslipped samples was used for analysis and reported here. After the tensile tests, SEM images were taken from top surface and fracture surfaces for microstructural analysis (Make: JEOL; Model: JXM 6400).

Figure 2: Tensile test setup used in the experiment

4.1.3. Phase identification

An X-ray diffractometer (Make: Phillips Norelco; Model: PW 1830) operating with Cu-Kα raidiation at a wavelength of 1.5418 Å was used to characterize the structure of the ribbons before and after laser irradiation.

4.1.4. Hardness measurement

The surface hardness across the laser track was measured using a Vickers microhardness tester (Make: Clark; Model: CM-700AT, illustrated in fig 3) with a normal load of 50 g and testing time of 15 s. The ribbons were supported on an aluminium plate to prevent pre-bending during hardness testing. For each sample, the microhardness was measured over 1.4 mm span. As the

width of the laser track was about 0.6 mm, it was made sure that each span of hardness measurement covered at least one laser track in the traverse direction.

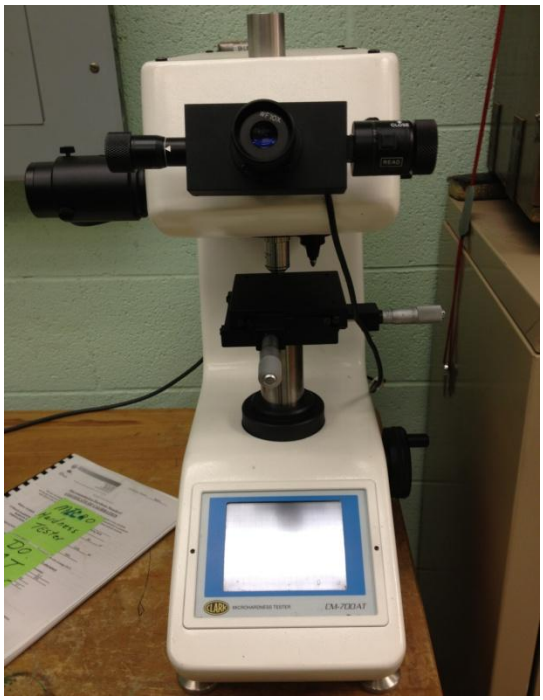

Figure 3: Hardness test setup used for microhardness measurement

4.1.5. Heat flow analysis

A differential scanning calorimetry analysis (Make: NETZSCH; Model: STA 449 F3 Jupiter) was conducted at a constant heating rate of 20 K/min to characterize characteristic temperatures and heat flow during heating for both as-received and laser irradiated ribbons.

4.1.6. Surface profile measurement

A 3D non-contact surface profilometer (Make: Nanovea; Model: PS50, illustrated in Fig. 4) was used to analyze the surface profile for untreated and laser irradiated samples. For each sample, an area of 8 mm × 3 mm was scanned to cover at least three laser tracks.

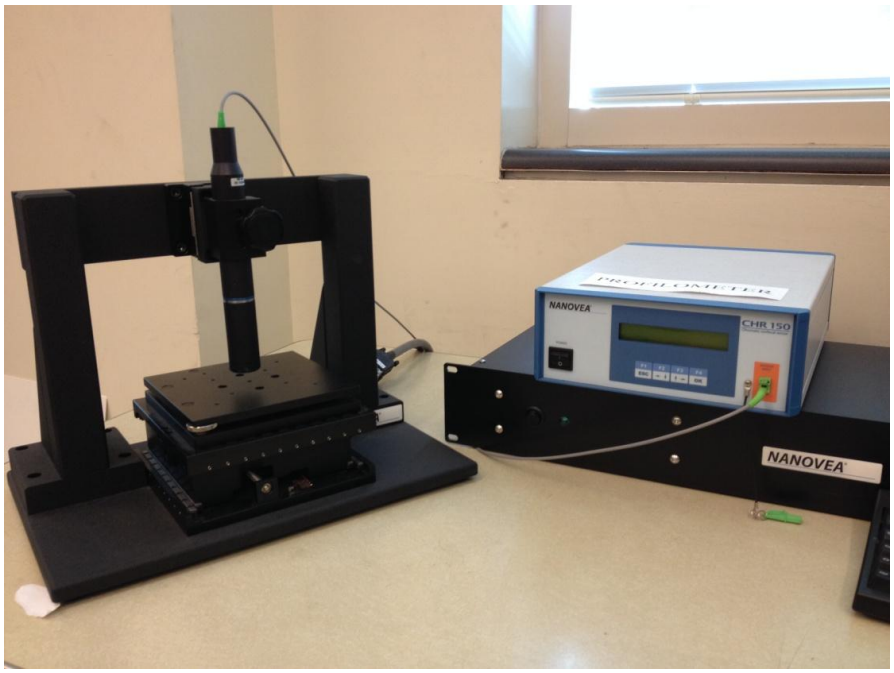

Figure 4: Nanovea optical 3-D profilometer used for measuring surface deformation

4.2. Thermal Analysis

The temperature distribution in the sample due to laser irradiation was obtained using thermal analysis. Comsol Multiphysics finite element analysis was used for the thermal analysis. The governing equation corresponding to heat transfer in solid was given by the following equation:

$$\rho C_P \left[\frac{\partial T}{\partial t}\right] = k\left[\frac{\partial^2 T}{\partial x^2} + \frac{\partial^2 T}{\partial y^2} + \frac{\partial^2 T}{\partial z^2}\right] \quad (1)$$

Here, ρ, C_p and k are defined as material density, specific heat and thermal conductivity respectively. The heat flux function was defined as following:

$$Q_{in} = \frac{(1-R_c)P}{\pi r^2}\, e^{\left(-\frac{(x-x_{00})^2}{2\sigma_x^2} - \frac{(y-y_0)^2}{2\sigma_y^2}\right)} \quad (2)$$

Here, P, r, R_c, σ_x and σ_y are defined as laser power, spot radius of laser beam, reflectivity of the material and standard deviation of laser heat source along x and y axes respectively. x and

y give the spatial position of point of interest, x_{00} and y_0 give the position of heat source. Table 1 summarizes all the laser parameters and material properties used in the simulation. One laser track was considered in the simulation, so width of the sample was taken as 3.6 mm. Convective and radiation heat loss were also taken into consideration, yet found to be negligible comparing with the heat input to the system (Fig. 6). Expression for convective and radiation heat fluxes are given by following equation:

$$Q_{convection} = h\,(T - T_{\infty}) \tag{3a}$$

$$Q_{radiation} = \varepsilon\sigma(T^4 - T_{\infty}^4) \tag{3b}$$

Table 1: Laser Parameter and material properties used in the thermal simulation [41, 48, 49]

Name of the parameters	Value of the parameters
Laser power, P	100 W
Spot radius, r	0.3 mm
Standard deviation in x-direction, σ_x	0.1 mm
Standard deviation in y-direction, σ_y	0.1 mm
Length of the sample, L	10 mm
Width of the sample, W	3.6 mm
Thickness of the sample, H	22.86 μm
Reflectivity, R_c	0.64
Convective heat transfer coefficient, h	2500 W/(m^2K)
Emissivity, ε	0.4
Stefan-Boltzman constant, σ	5.67 x 10^{-8} W/(m^2K^4)

Here, h, ε and σ are defined as convective heat transfer coefficient, emmisivity and Stefan-Boltzman constant respectively. T and T_∞ are denoted as instantaneous and initial temperature respectively. Figure 5a shows the schematic diagram used in the simulation. The brown block is the sample holder. Blue strip is the sample which is subjected to irradiation. The sample holder was made of copper. Since copper is thermally conductive, conduction was assumed between the sample and holder. All the remaining surfaces were subjected to convection and radiation heat loss. Initial temperature was assumed to be ambient temperature (T_∞). Absorption coefficient of the system was taken as of iron and therefore, the attenuation length was found to be 0.0192 μm. Since it is much smaller than the sample thickness, it was believed that most of the irradiation and corresponding increase in temperature occurred at surface and near surface region. Similar pattern was found in the simulation for temperature distribution along the depth (not shown here). The track shown in the blue strip in Fig. 5a along x-axis represents the path of heat source. Boundary condition for the laser track was given by following equation:

$$k\left[\frac{\partial T}{\partial y}\right] = Q_{in} - Q_{convection} - Q_{radiation} \quad (4)$$

Since motion of heat source was one dimensional (x-axis), change in the heat source position with time was incorporated in the model through the following equation:

$$x_{00} = x_0 + Ut \quad (5)$$

x_0 is the starting position of heat source when time is zero, U is the scanning speed and t is time. Boundary condition for remaining top surface and side surfaces was as follows:

$$k\left[\frac{\partial T}{\partial y}\right] = -Q_{convection} - Q_{radiation} \quad (6)$$

Figure 5b shows the mesh distribution of the system. Triangular mesh elements were chosen for the system with a swept style along the thickness. Mesh density for the system other

than the laser track was chosen to be lower in order to reduce computational time. To obtain the spatial temperature and heat flux profile at the surface, a line parallel to y-axis was chosen at x = 1.35 mm. Heating and cooling rate, thermal stress at the surface were taken corresponding to a point at x = 1.35 mm, y = z = 0.

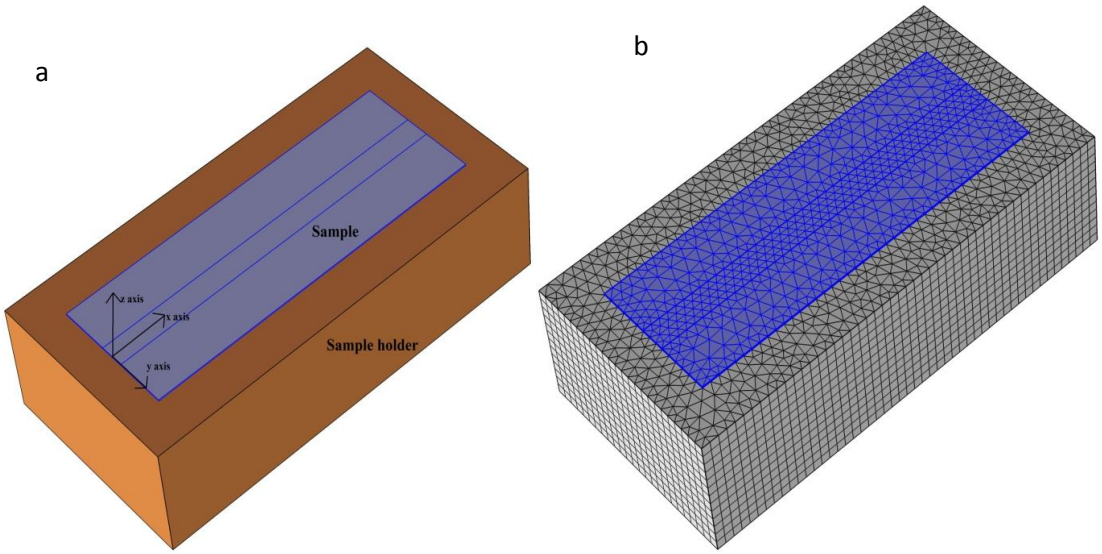

Figure 5: Model used in the simulation: **(a)** Schematic diagram, and (b) mesh distribution of sample with sample holder.

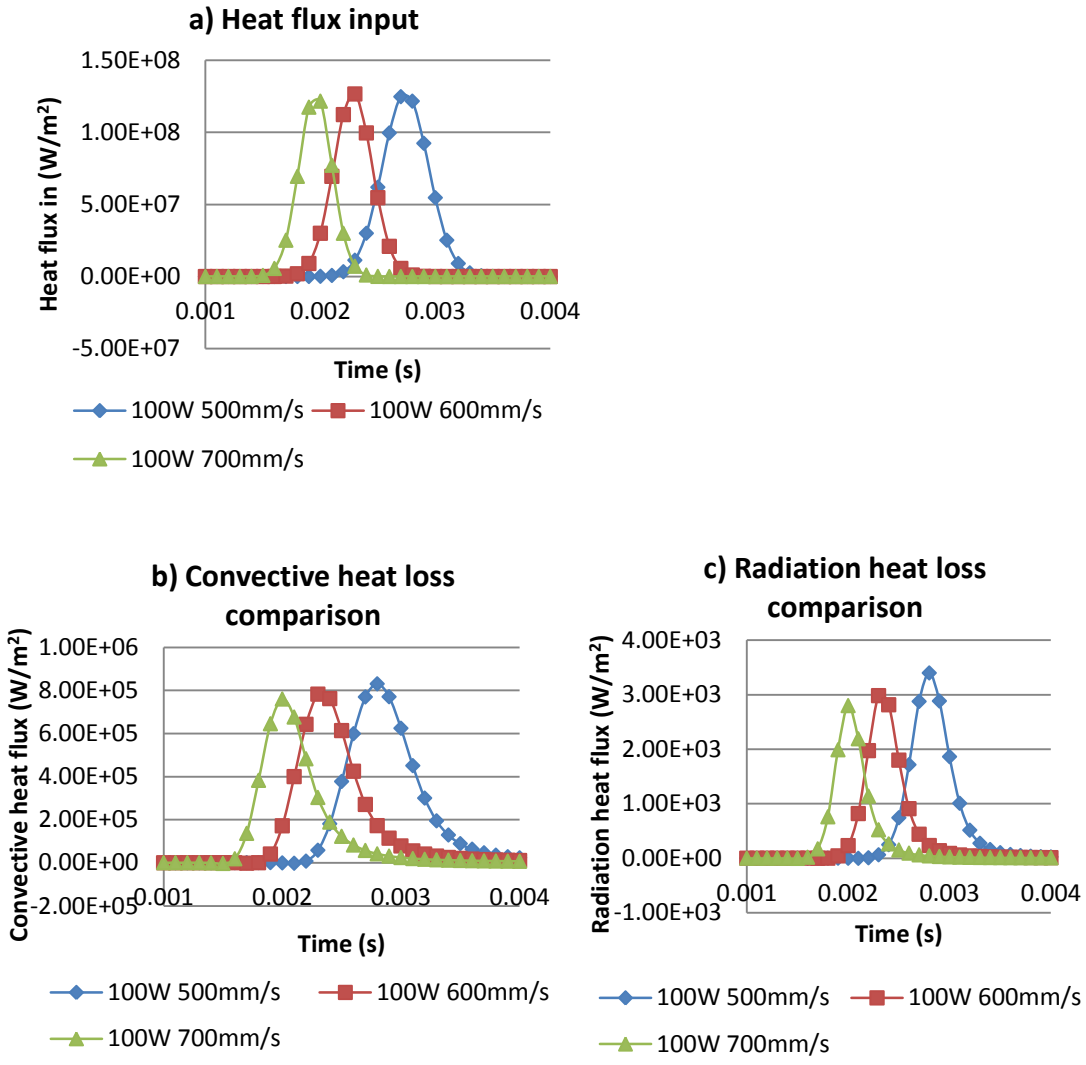

Figure 6: Heat flux and heat loss due to laser irradiation of the ribbons: (a) Heat flux input for the laser irradiated samples, (b) convective heat loss was found to be only in the order of 0.1 % of the heat input, and (c) radiation heat loss was only in the order of 1% of convective heat loss.

CHAPTER 5

RESULTS AND DISCUSSIONS

5.1. XRD analysis

Figure 7 shows XRD patterns for as-received and laser irradiated ribbons. The XRD pattern for as-received ribbon shows a broad halo peak at $2\theta = 45^{\circ}$. No sign of sharp crystallographic peaks was observed in the pattern, indicating fully amorphous structure of as-received ribbons. Similar patterns exhibiting broad halo peaks were also observed for laser irradiated samples. The presence of diffused halo peak for the laser irradiated samples indicated retention of amorphous structure in the samples. An increase in intensity of the halo peak was also observed for the samples irradiated with all laser scanning speeds. The increase in intensity was minimal for the fastest laser scanning speed (700 mm/s). Significant increase in intensity of broad halo peak was observed for the samples scanned with slower scanning speeds (500 and 600 mm/s). This increase in intensity of the diffused peak for the laser irradiated samples can be associated with improved atomic order. It seems that the thermal energy due to laser irradiation initiated atomic movement, but the movement was not sufficient enough to form fully defined crystallites. Formation of such ordered regions in the amorphous matrix play a significant role in the subsequent crystallization process [50].

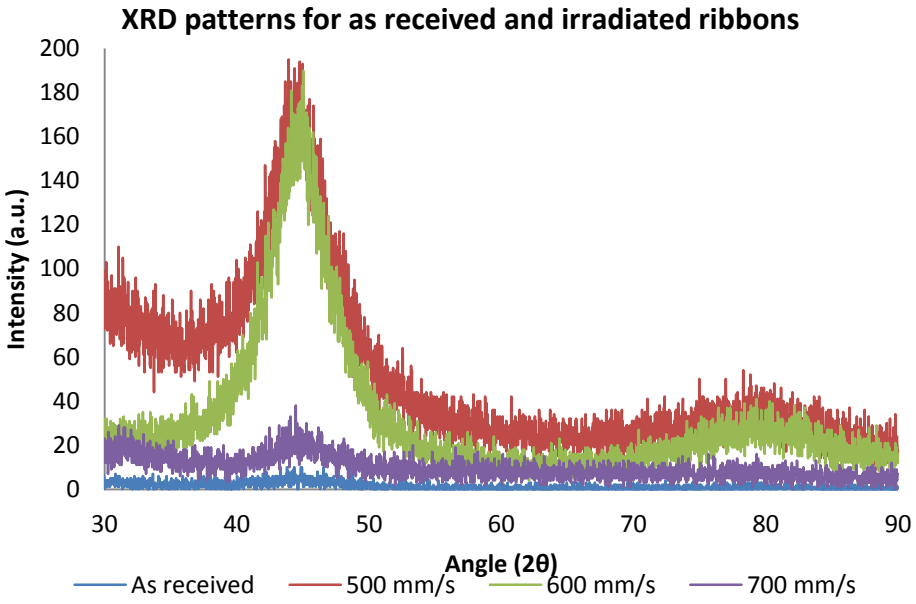

Figure 7: XRD patterns for as received and irradiated ribbons.

5.2. Microstructural Analysis

Figure 8 shows the microstructures from the surface for as-received and laser irradiated (scanned with 500 mm/s) ribbons. The as-received and laser irradiated samples exhibited similar surface microstructure marked by the presence of surface defects typical of melt spinned ribbons. No indication of profuse surface crystallization was observed for the laser irradiated samples, corroborating the XRD observations that amorphous structure was retained in the laser irradiated samples. Various thermo-physical effects that can retain the fully amorphous structure during laser interaction with amorphous material are: a) surface ablation, b) surface remelting and resolidification and c) surface heating below crystallization temperature. The absorption of laser radiation at the surface causes localized heating, resulting in temperature rise. The thermal (evaporative) and/or non-thermal (direct solid to vapor) ablation results in removal of material at the surface, forming well defined holes or grooves. No such features were observed on the laser irradiated samples, ruling out the possibility of surface ablation in the present work. If the surface

is heated above the melting point of the material, the subsequent rapid resolidification can retain amorphous structure. However, surface recast layer, typical characteristic of resolidification, was not observed in the laser irradiated samples. Based on XRD and surface microstructure analysis, it seems that the laser irradiation resulted in surface heating below crystallization temperature of the amorphous alloy. The thermal analysis (discussed in detail in latter sections) also indicated that the peak temperature at the surface reaches about 320-360 °C (depending on laser scanning speed) that is well below the crystallization temperature of the alloy. Thus, the retention of amorphous structure at the surface of the laser irradiated amorphous ribbons is primarily due to laser surface heating below the crystallization temperature of the alloy.

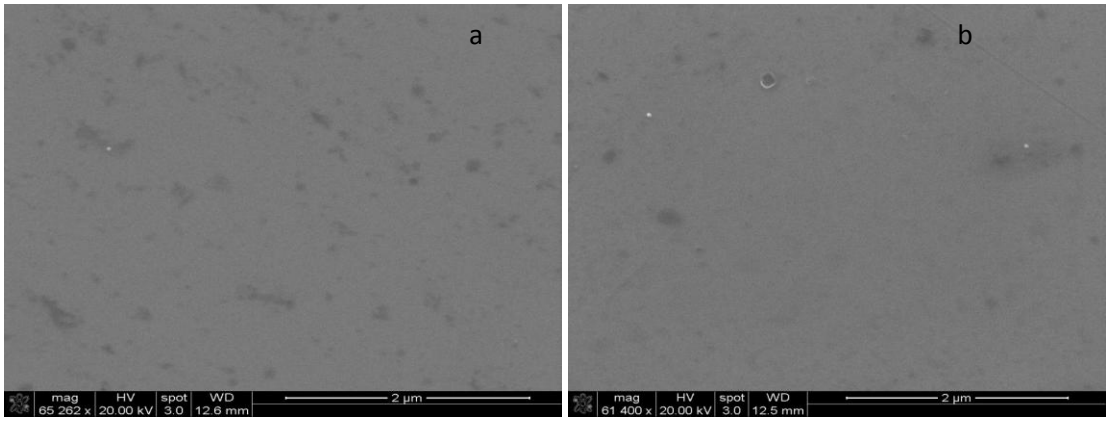

Figure 8: SEM images of the top surface: (a) as-received, and (b) irradiated ribbon 500 mm/s speed.

Figure 9 shows the fracture morphology of the as-received amorphous ribbon after tensile fracture. The fracture surface revealed river-like pattern with cellular features (indicated in small circles) between the river marks. Similar fractures were reported for Fe-Si-B amorphous system subjected to tensile load [51, 52]. Two regions were observed at the fracture surface in the reported literatures. Periodic striation pattern with finer cells was reported in the first zone (stated as mirror zone) while river pattern with larger cells was reported in the second zone. Second region was reported as a result of crack branching at very high crack propagation velocity which

appeared at the final stage of failure. Since river pattern with cellular feature was observed in the present study, it referred to the second region in the reported literature. The cellular microstructure observed in Fig 9 is often referred to as damage cavities or microvoids. Similar microstructure was observed not only in Fe-based amorphous system, but also in other amorphous structures [53] as well. It was suggested that the appearance of such microvoids did not depend on chemical composition, rather depended on amount of free volume and atomic density fluctuation at nanometer level.

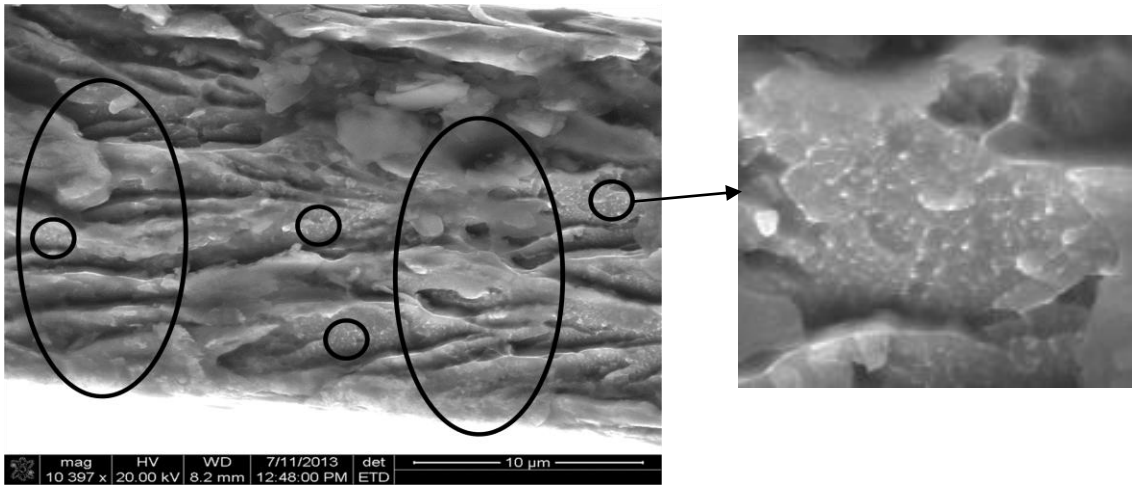

Figure 9: Fracture surface of as-received ribbon.

Figure 10 and 11 show fracture surface for the laser irradiated ribbons. In all cases, river pattern with cellular morphology was observed, which was identical with as-received ribbon. 7b shows a clear image of the cellular morphology. Average cell diameter was calculated as 205 nm for 700 mm/s, so the approximation taken for as-received ribbon was reasonable. Cell sizes for 500 and 600 mm/s were also approximated to 200 nm, since magnified images for 500 and 600 mm/s could not be obtained.

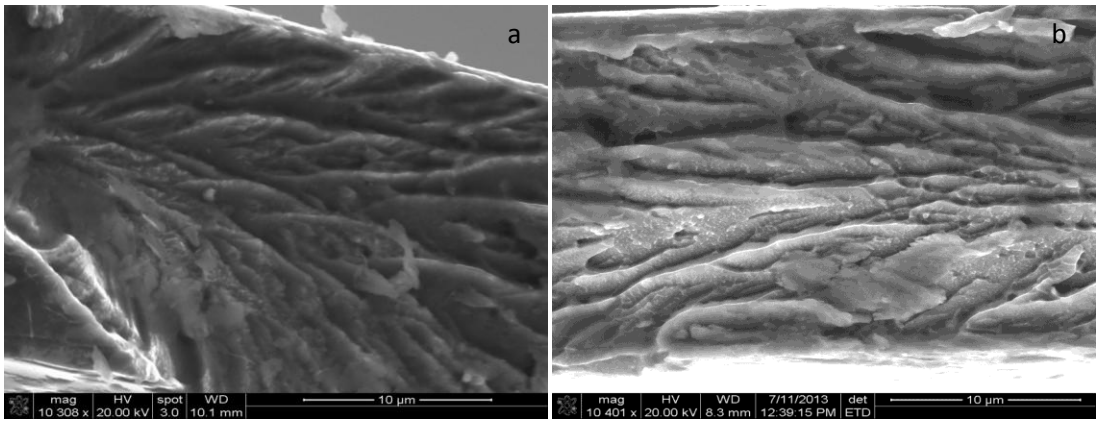

Figure 10: Fracture surface of irradiated ribbons: (a) 500 mm/s, and (b) 600 mm/s scanning speed

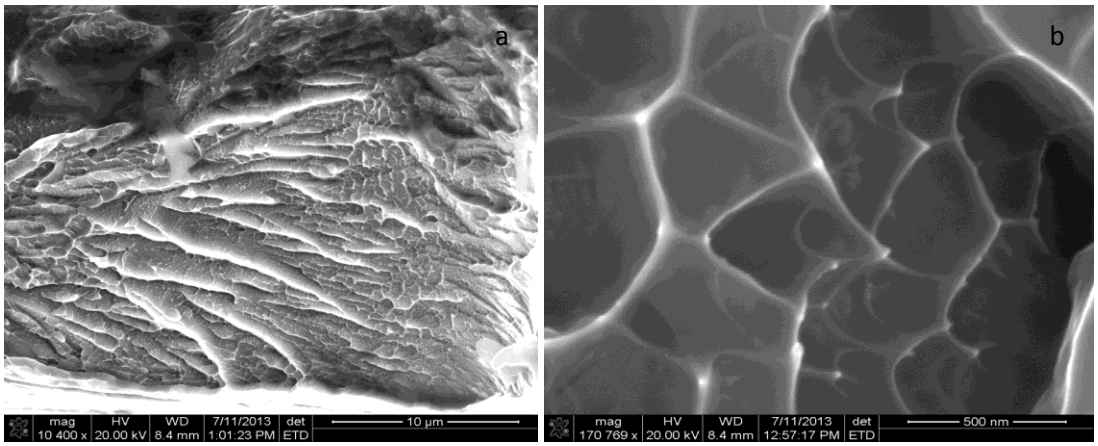

Figure 11: Fracture surface of irradiated ribbon: (a) 700 mm/s scanning speed, and (b) a magnified version of cellular structure

5.3. Differential scanning calorimetry (DSC) analysis

The DSC traces for as-received and laser irradiated (with three scanning speeds) samples are presented in Fig. 12. All the heat flow DSC traces showed two depressions, indicating two-stage crystallization. The first depression at about 510 °C and the second depression at about 550 °C indicate formation of of α-Fe and Fe_2B respectively.

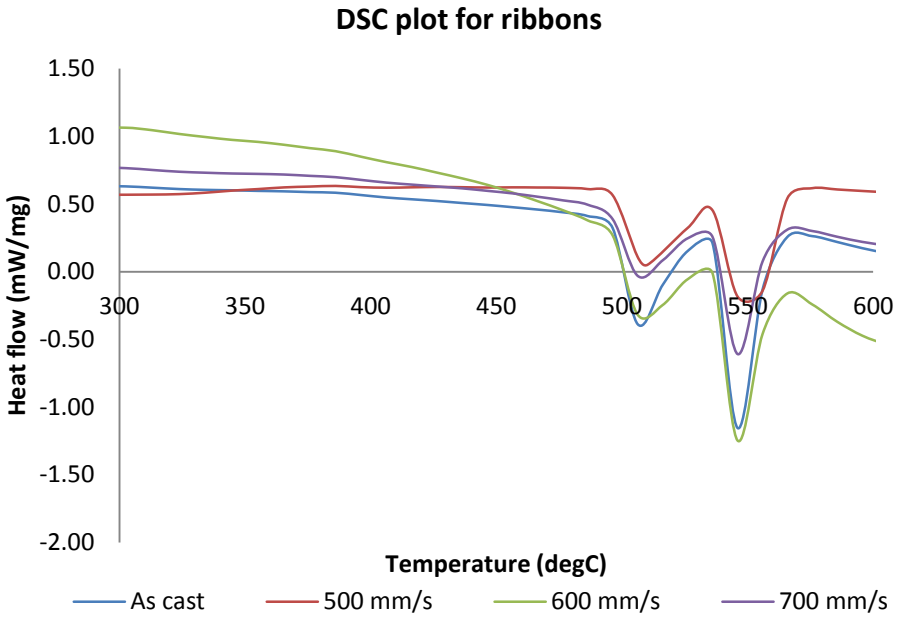

Figure 12: DSC result of as-received and heat treated ribbons.

The area under depression represents enthalpy of crystallization. Table 2 summarizes the enthalpy of crystallization and crystallization temperature for as-received and laser irradiated samples. It appears that the area under depression for laser irradiated samples differ from the as-received sample. According to Beukel *et al* [54], two amorphous alloys with same composition will have same area under the peak or depression in DSC plot if the initial free volume for these two systems is same. Their investigation included annealing of Pd-based amorphous structure in such a way that different samples contain same amount of free volume, although annealing time and temperature were different. DSC curve for their samples showed same peaks for all the cases. Similar results were observed in Ti-based amorphous structure as well [55]. So, change in area under depression among the samples in present work clearly indicates difference in initial free volume for laser irradiated sample compared with as-received one. It is a well established fact that amorphous ribbon undergoes structural relaxation or crystallization through change in their free volume [56]. Upon heating, atomic mobility and rearrangement are enhanced at heating. This

finally results in change in their free volume [57]. This indicates that the change in enthalpy is associated with crystallization or relaxation for the laser irradiated ribbons. But no well defined crystallographic peak was observed from XRD pattern analysis. Therefore, it can be stated that the change in enthalpy observed in DSC occurred due to structural relaxation.

Table 2: Summary of DSC experiment

Laser condition	First crystallization temperature (^{0}C)	Enthalpy of first crystallization (J/g)	Second crystallization temperature (^{0}C)	Enthalpy of second crystallization (J/g)
As-received	511	36.54	552	52.64
500 mm/s	510	32.13	551	46.93
600 mm/s	510	30.19	548	41.71
700 mm/s	509	24.95	547	34.74

Change in crystallization enthalpy with laser scanning speed was another result from heat flow, summarized in Table 2. In the table, it is evident that enthalpy decreased with increase in scanning speed. It is widely known that rate of change of enthalpy (H) is proportional to the rate of change of average free volume per atom (v_f) [54]. Table 3 shows the trend for thermal energy and change in enthalpy with laser scanning speed. Thermal energy for irradiation was calculated by the following equation [58]:

$$I = \frac{P}{vD} \tag{7}$$

Here, I is defined as heat energy per unit area, P as laser power, v as scanning speed and D as spot diameter. Since all the parameters except laser scanning speed were kept constant during laser irradiation, thermal energy was inversely proportional to the scanning speed. From Table 3, it is clear that thermal energy decreased and change in enthalpy increased with increase

in laser scanning speed. It is based on the fact that thermal energy was lower at higher scanning speed, so atomic mobility was expected to be lower. This slower atomic movement or rearrangement caused smaller change in total free volume, allowing higher amount of free volume available during crystallization. Since change in free volume is proportional to the change in enthalpy, change in free volume during crystallization caused higher change in enthalpy for sample irradiated with higher scanning speed. This observation can also be explained by Johnson-Mehl-Avrami equation [59-62], stated as follows:

$$x = 1 - e^{(Kt)^n} \tag{8}$$

$$\text{where, } K = K_0 e^{-\frac{E_g}{RT}} \tag{9}$$

Here, x is defined as volume fraction of transformed crystal, K as reaction rate, K_0 as frequency factor, t as time, E_g as activation energy, R as gas constant and T as annealing temperature at which crystal forms. n is denoted as Avrami constant, associated with crystallization mechanism of a particular crystal in a given system. Avrami constant for α-Fe formation was reported as 3, which states it's formation is controlled by short range diffusion [46]. Since average free volume per atom was lower at lower laser scanning speed, it made diffusion difficult to occur. Therefore, crystallization enthalpy was observed higher at lower laser scanning speed.

Table 3: Trend for thermal energy and change in enthalpy with scanning speed

Process parameter	Thermal energy (J/mm^2)	Change in enthalpy, ΔH (J/g)
500 mm/s	0.33	4.41
600 mm/s	0.28	6.35
700 mm/s	0.24	11.59

Shift in crystallization temperature for laser irradiated samples is another observation obtained from Table 2 and Fig. 12. Crystallization temperature decreased with increase in laser scanning speed. Shift in crystallization temperature is associated with shift in activation energy [57]. Liu *et al.* calculated activation energy for α-Fe and Fe_2B by Kissinger method and reported as 260 kJ/mol and 308 kJ/mol respectively [63]. In another study, Mehta *et al.* showed decrease in activation energy for ion irradiated Fe-based amorphous ribbon [64]. They reported this decrease in activation energy was due to an increase in the density of defect state after irradiation. Furthermore, according to the study conducted by Cabral-Prieto *et al*, concentration of defect increases at crystallization temperature. In present study, average free volume per atom was higher for the sample irradiated at higher laser scanning speed. As a result, concentration of defect was expected to be higher at crystallization temperature during DSC analysis. This caused crystallization process easier to occur. Therefore, activation energy was reduced, resulting in a drop in crystallization temperature.

Two types of relaxation process are known for amorphous system: Topological Short Range Ordering (TSRO) and Compositional Short Range Ordering (CSRO). Unlike CSRO, TSRO concerns relative position of the atoms, regardless their chemical composition. So, this is a direct result of change in free volume, while CSRO can be obtained from change in viscosity. Change in area under depression/peak in DSC plot is attributed to change in free volume, where CSRO has little effect than TSRO. Change in enthalpy was prominent in the obtained DSC result. Therefore, it can be deduced that relaxation process was mostly associated with TSRO in the irradiated samples.

5.4. Thermal embrittlement

Figure 13 shows stress-strain relationship for as-received and laser irradiated ribbons. Linear relation between stress and strain was observed for all the cases. Despite the fact that all the

ribbons showed brittle failure, the area under the stress-strain curve was different for laser irradiated samples, indicating thermal embrittlement due to laser irradiation. Figure 14 shows change in fracture stress and strain after irradiation. Significant reduction was observed in both cases with decrease in laser scanning speed. Reduction in fracture strength (Fig 14a) and strain (Fig 14b) for 500 mm/s was more than 50%, indicating significant embrittlement upon laser irradiation. Several explanations associated with thermal embrittlement of amorphous alloy have been reported till to date. Each explanation was studied and best answer for the present case was chosen through process of elimination.

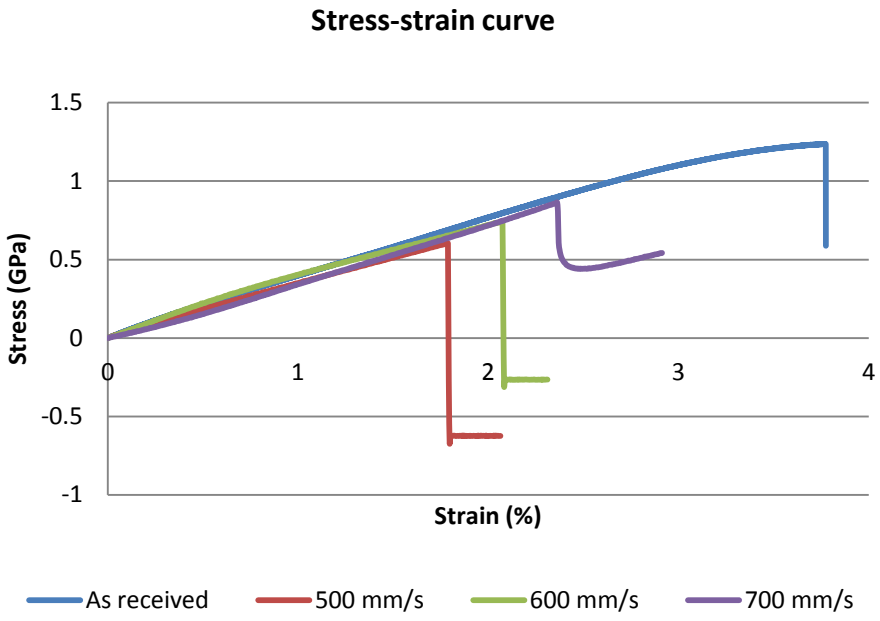

Figure 13: Stress-strain curve for the ribbons

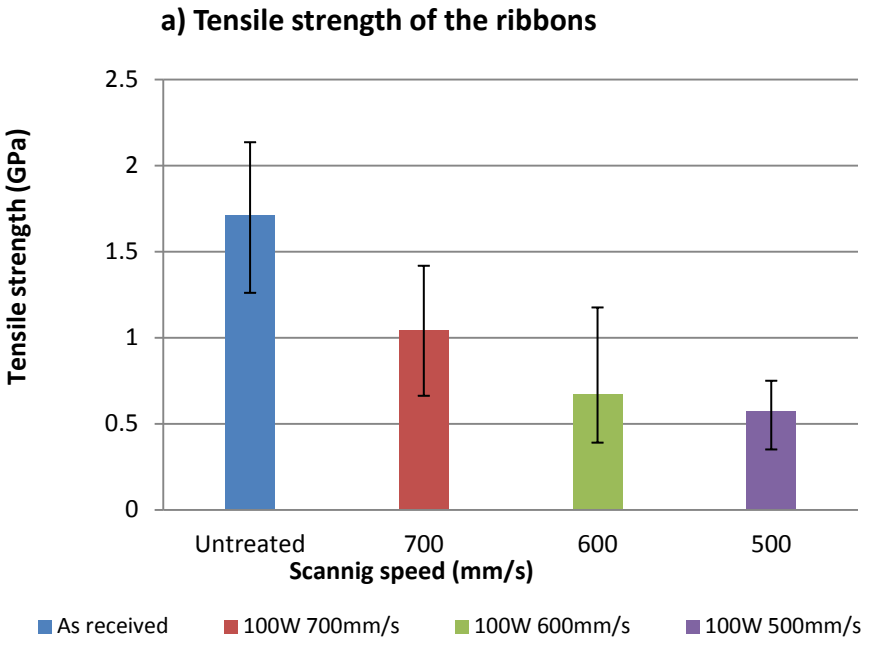

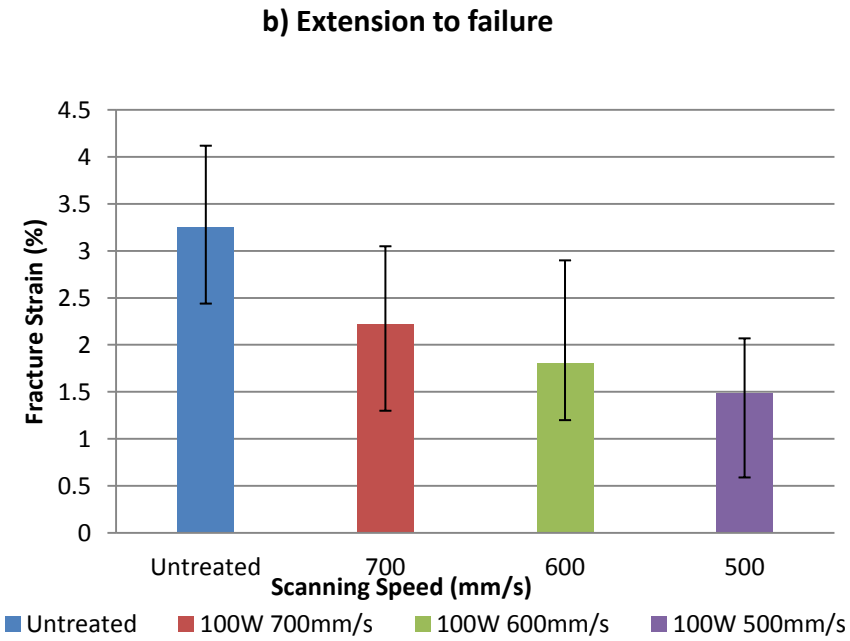

Figure 14: Thermal embrittlement of irradiated samples

Thermal embrittlement is greatly influenced by crystal formation. It was found through previous study [29] that free volume is maximum at the time of crystallization, associated with large atomic movement. This large atomic movement and associated change in free volume can play significant role in thermal embrittlement. Furthermore, formation of new crystalline phase may induce embrittlement of the ribbon. It was reported that formation of α-Fe upon crystallization is responsible for embrittlement of Fe-Si-B system [45]. But this was the least expected case to happen in the present study, since no clear sign of crystal formation was observed from SEM and XRD pattern analyses for laser irradiated ribbon. This led towards cancelling out the possibility of crystal formation and embrittlement associated with it.

Thermal embrittlement for amorphous structure can also be associated with separation of two amorphous phases. This phenomenon was revealed through small angle X-ray scattering for Fe-based amorphous systems [65, 66]. It is worthwhile to analyze this case for present study since no crystallographic peak was observed in the XRD patterns for laser irradiated ribbons (Fig 7). Phase separation is enhanced in the presence of phosphorous or boron elements [67]. In an Fe-Ni-B system [65], it was reported that upon annealing, two amorphous phases were formed, a-(Fe,Ni,B) and a-$(FeNi)_3B$. The boron-rich phase appeared to be brittle enough to make the whole system brittle. Minimum volume fraction of the boron-rich phase for inducing embrittlement was reported to be 30%. Even though Boron was one of the constituent elements in the present study, this case was unlikely to happen. In the reported study, Boron content was significantly higher than the present alloy. While 20% of Boron was present in the reported alloy, present alloy contained only 1-5% of Boron. This made the formation of Boron rich phase required for embrittlement more difficult. Furthermore, the phenomenon of segregation of amorphous phases varies widely from alloy to alloy. Thermal embrittlement of $Fe_{79.3}B_{16.4}Si_4C_{0.3}$ amorphous alloy was reported not because of phase separation [68], even though Boron content was high. Electron density fluctuation obtained from small angle X-ray scattering was not significant enough to

identify existence of different amorphous phase at a temperature below crystallization point. Another study by Fish and Child [69] on annealed Fe-B amorphous alloy did not clearly reveal phase separation. Based on these arguments, phase separation was unlikely to happen for present study.

As mentioned earlier, the heat source used in the present study had Gaussian distribution in nature. As a result, spatial distribution of heat flux was observed across the laser track (Fig 18a). This led towards different thermal expansion in the spatial direction. Difference in thermal expansion had been reported responsible for thermal embrittlement in Fe-based amorphous ribbons [70]. According to Kumar *et al,* HREM image analysis revealed BCC type local short range ordering embedded in an amorphous matrix for $Fe_{78-x}Ni_xSi_{10}B_{12}$ amorphous ribbon. Thermal expansion coefficient of these two regions was different. So, upon annealing, these two regions experienced different thermal expansion and thermal stress. During cooling this led towards residual stress and caused embrittlement if the stress was higher than critical fracture stress. Since presence of BCC cluster is a sign of inhomogeneity, thermal embrittlement was reported as a result of stress caused by structural, compositional or other kind of inhomogeneities. As HREM image was not available for present study, presence of BCC type clusters could not be revealed. But difference in thermal expansion was evident from thermal simulation (Fig 18). In addition to difference in thermal expansion, short range ordering of Fe-Si-B systems upon annealing was reported to be responsible for embrittlement by other researchers [20, 71]. This short range ordering was associated with densification and loss of quenched-in free volume during annealing. Composition of the reported alloy systems was similar to the present alloy system. Furthermore, TSRO was evident from heat flow analysis revealed by change in enthalpy. This emphasizes the possibility of thermal embrittlement for present alloy by SRO. A positive correlation was found between developed thermal stress and change in free volume (see section

5.6). So, based on the above discussions, it can be stated that short range ordering was responsible for early failure under tensile load in the present study.

5.5. Microhardness

Figure 15 shows microhardness variation for as-received and laser irradiated samples over 1400 micron span for each specimen. Since the width of the laser track was smaller (600 micron) than the selected span, each plot for laser irradiated sample (15b, 15c and 15d) fully covered heat treated area and some part of untreated area. Before doing any analysis on microhardness variation, indent depth to sample thickness ratio was calculated to check the effect of substrate. For Vickers Microhardness test, indent depth is assumed to be 1/7 of the diagonal length of the indent. The diagonal length is measured from the following equation [72]:

$$\mathrm{VHN} = 1.854\ \frac{\mathrm{F}}{\mathrm{d}^2} \tag{10}$$

Here, VHN is the H_v value obtained from Fig 15, F is the indent load in kgf and d is the mean diagonal indent length in millimeter. Indent depth was measured from d and indent depth to sample thickness ration was found to be 15 for all the cases (Fig 15a-d). Therefore, measured microhardness values were free from any substrate effect. Table 4 summarizes the result from Fig. 15. In the table, the unit of microhardness is converted into GPa in order to compare it with the work done by other researchers. Microhardness for as-received alloy was found to be as high as 8.58 GPa, which stayed close to the result (8.6 GPa) obtained by Cabral-Prieto *et al.* [29]. Microhardness for laser irradiated ribbons was found to be very close to that of as-received ribbon. Only 5% increase was observed for 500 mm/s, where as 4% increase in microhardness was observed for 600 mm/s. In their study, Cabral-Prieto *et al* conducted annealing of Metglas 2605SA1 alloy over a wide range of temperature through furnace heating and analyzed the results obtained from microhardness and Mössbauer Spectroscopy (MS). Microhardness was reported as high as 12 GPa for the sample annealed at 100 °C for 20 minutes, followed by a decrease. This

decreasing trend was observed up to annealing temperature of 360 °C, where the microhardness was minimum (around 8.5 GPa). Reported microhardness at 360 °C was very close to that of as-received ribbon. After that, H_v values started to increase again with annealing temperature and this trend followed till glass transition temperature was achieved. They reported that the minimum value of microhardness for annealed ribbon did not occur for crystallization, since the temperature was significantly below the crystallization point. Reported MS study showed variation in magnetic domain orientation with thermal treatment, revealed by change in the line-area ratio in their MS plot. Line-area ratio for unheated ribbon and ribbon annealed at 360 °C was found to be very close to each other (2.72 for unheated and 2.70 for annealed ribbon), suggesting that magnetic domain orientation for these two conditions was similar. So, they explained the similarity in microhardness for these two conditions was mainly due to similarities in magnetic domain orientation.

In order to relate present study with the one obtained by Cabral-Prieto *et al.*, determination of temperature during irradiation was necessary. Figure 16 illustrates spatial distribution of temperature across the laser track, obtained from thermal simulation. Temperature rise because of laser irradiation stayed within the range of temperature reported by Cabral-Prieto *et al.* While their reported minimum microhardness was obtained at 360 °C, temperature during laser irradiation in present study stayed between 325 °C to 360 °C. So, temperature range and microhardness value came with good agreement with the reported value. Therefore, the similarity in microhardness between laser irradiated and as-received sample was mainly due to similarity in magnetic domain orientation between the two sample types. The slight increase in microhardness for the samples irradiated with 500 and 600 mm/s laser scanning speed was possibly because of change in free volume occurred during irradiation.

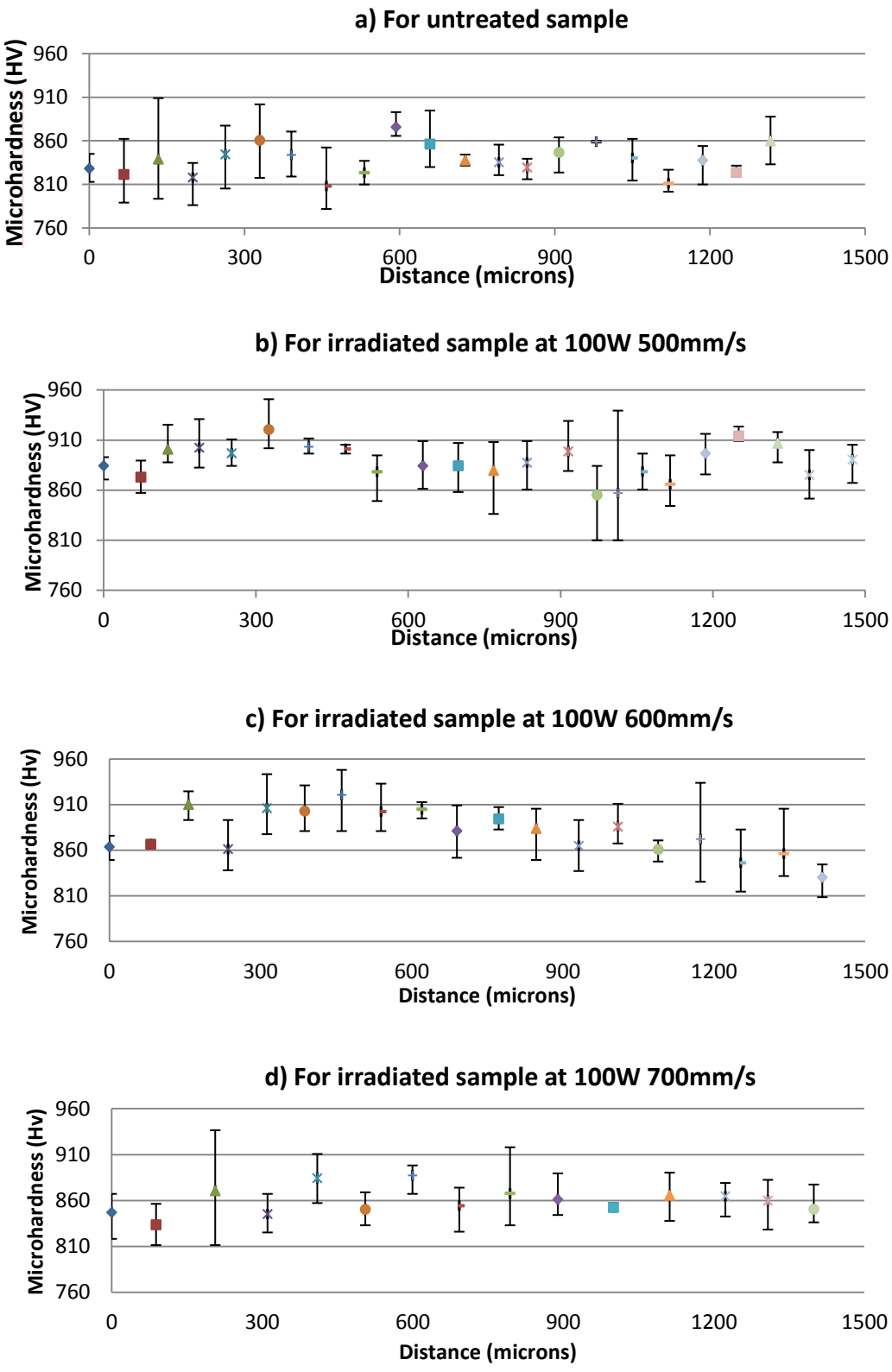

Figure 15: Variation of microhardness over a 1400 micron span

Table 4: Summary of microhardness result

Condition	Vickers number	Microhardness in GPa
As-received	810-875	7.94-8.58
500 mm/s	850-920	8.33-9.02
600 mm/s	830-910	8.14-8.92
700 mm/s	830-885	8.14-8.68

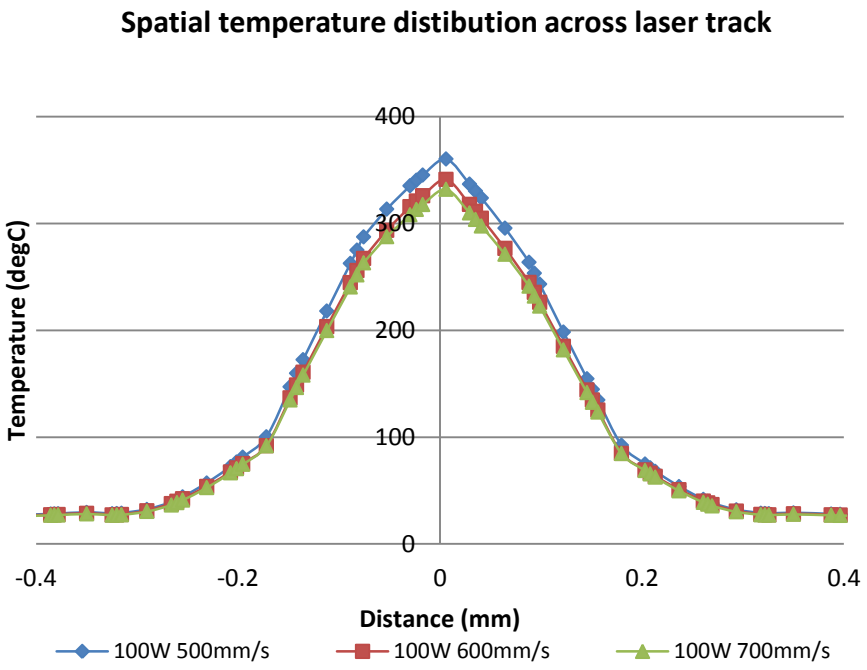

Figure 16: Temperature distribution during irradiation.

5.6. Surface profile

Figure 17a-d show variation in surface profile after laser irradiation. While surface of as-received (Fig 17a) ribbon shows an irregular profile with no specific trend, profile for laser irradiated surface show significant buckling along laser tracks (Fig 17b-d). For all laser scanning speeds, the

vertical deformation for buckling was around 5 μm from the mean surface level. Temperature variation for different laser scanning speed did not vary to a great extent (30 °C between the highest and lowest speed), resulting in similar vertical deformations for all the cases. While buckling for 500 and 600 mm/s was uniform along the laser track (Fig 17b and 17c), buckling for 700 mm/s was not uniform (Fig 17d). One possible reason is due to high scanning speed, heat transfer between heat source and the sample was not uniform at 700 mm/s. As a result, buckling was not completely developed in this case. Buckling occurred toward the heat source for 500 and 700 mm/s (Fig 17b and 17d). For 600 mm/s, buckling occurred away from the heat source (Fig 17c). Bending direction can be influenced by pre-bending condition, pre-existing residual stresses or counter bending due to thermal gradient [39]. Some laser tracks in 600 mm/s also showed upward bending (not shown in the figure). Buckling mechanism will be explained in the following section with the help of thermal history obtained from simulation.

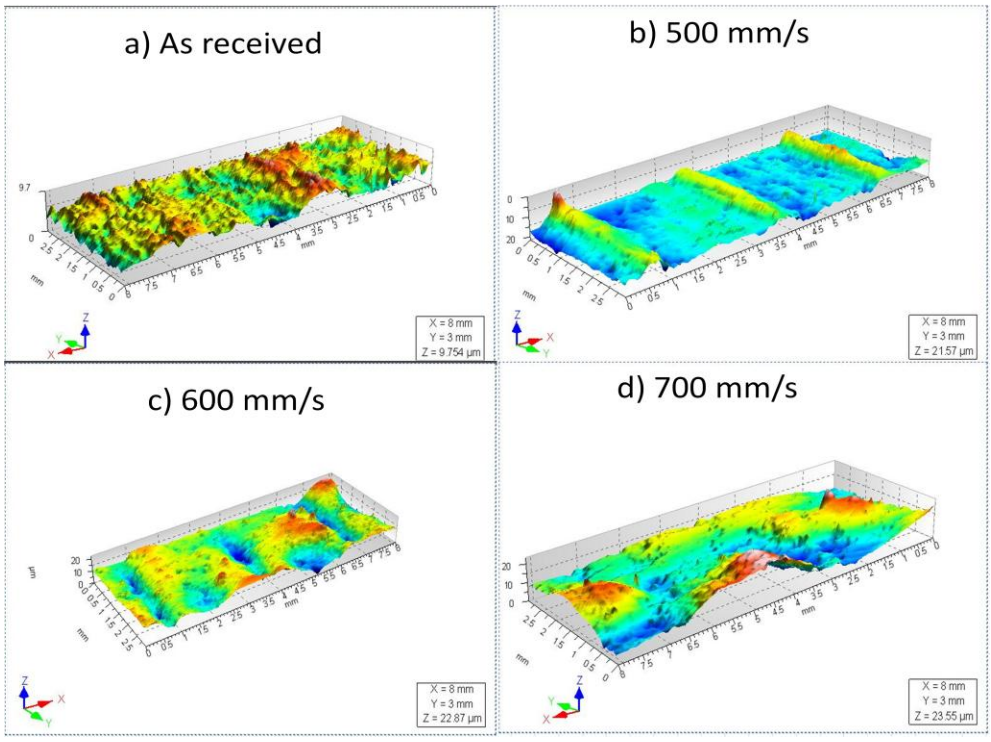

Figure 17: Variation in surface profile

As mentioned earlier, the heat source used in the present study had Gaussian distribution. So, laser intensity was maximum at the center of heat source and exponentially decayed towards the periphery. Similar distribution in the heat flux across the laser track is observed in Fig 18a. Since similar distribution was observed for all laser scanning speeds, result for 500 mm/s scanning speed is shown here for illustration purpose. Heat flux is showing normal distribution with 120 W/mm^2 in the middle. Similar pattern was found in the spatial temperature profile. A 2D image of temperature profile at the surface for sample irradiated with 500 mm/s scanning speed is illustrated in Fig 18b. The trailing effect represents the motion of heat source. From Fig 18b, it is clear that different areas in the heat affected zone experienced different temperatures. As a result, thermal expansion of these areas was different. Temperature was highest at the center, corresponding thermal expansion was maximum. During heating, all the areas experienced thermal expansion, so corresponding thermal strain and stress were tensile in nature. Figure 19 shows time dependent thermal stress at a point which is directly under the center of the heat source. Thermal stress is calculated from the following equation:

$$\sigma_{thermal} = \frac{E\alpha\Delta T}{1-\upsilon} \tag{11}$$

Here, E is defined as modulus of elasticity, α as thermal expansion coefficient, ΔT as change in temperature, and ν as Poisson's ratio. Since all the parameters in equation 11 are constant except thermal gradient, thermal stress is proportional to the thermal gradient. This resulted in an increase in thermal stress with decrease in laser scanning speed, since temperature was higher at lower speed. During heating, thermal gradient was positive. So, corresponding thermal stress was tensile. Tensile stress was maximum when heat source was about to leave the point. After that, rapid cooling began, resulting in decrease in thermal gradient. As ΔT approached to zero, thermal stress was reduced to zero. Since no other load was applied to the system, this thermal stress was responsible for buckling.

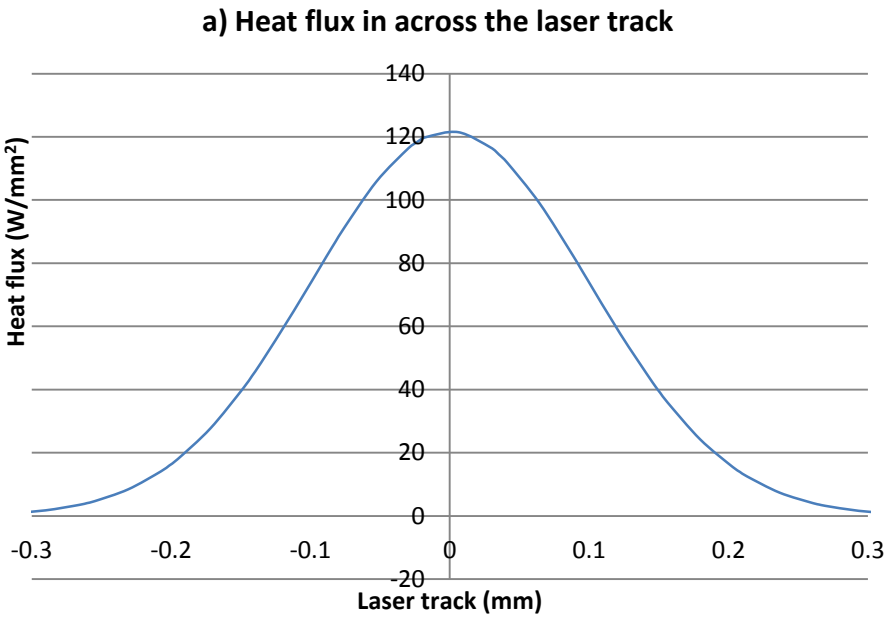

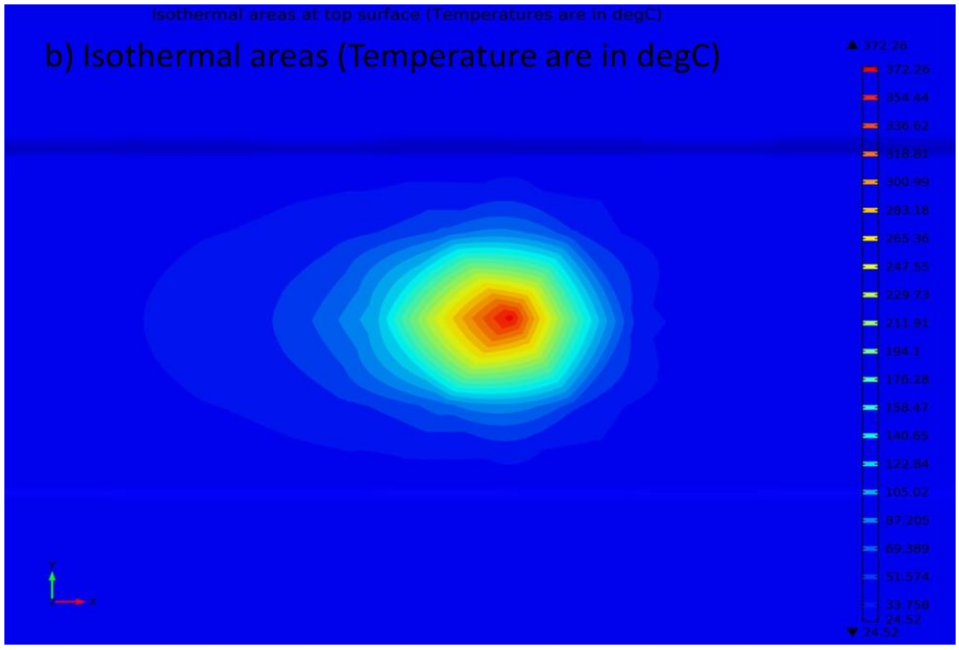

Figure 18: Thermal profile for 500 mm/s obtained from simulation.

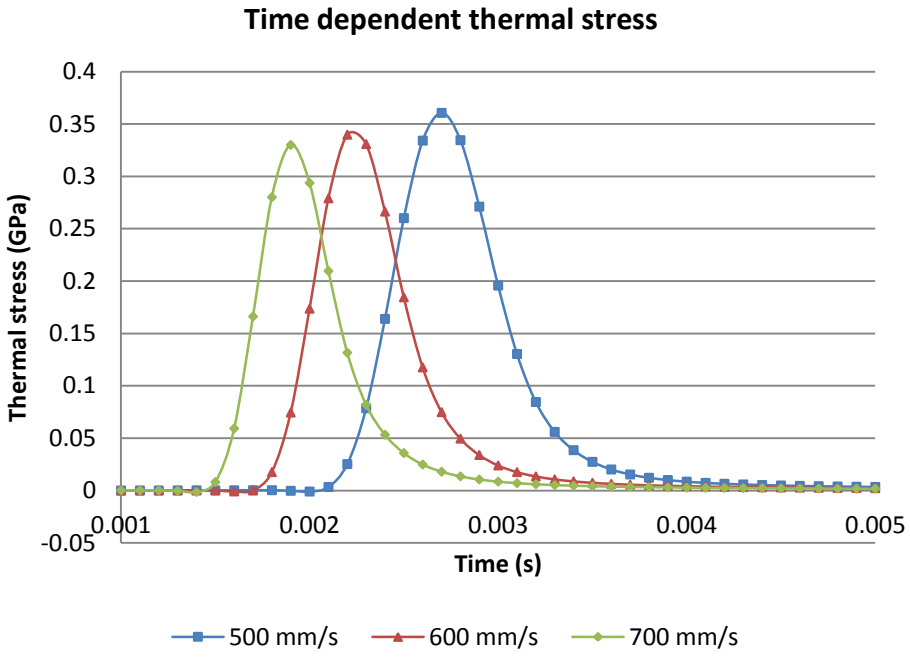

Figure 19: Time dependent thermal stress in the middle of laser track

During heating, free expansion of the heat affected zone was restricted by surrounding material. Since thermal stress was tensile in nature, counteracting stress applied by the surrounding was compressive in nature. Buckling occurred when this stress exceeded a certain value. Buckling is enhanced in case of thin metal and where temperature dependent flow stress is not too low [73]. Once a buckle was developed, it proceeded further due to thermal expansion in the subsequent areas. Since vertical deformation for all the laser irradiated ribbons was similar, distortion angles were measured to see the extent of deformation from a different perspective. Distortion angle for each laser scanning speed was measured from Fig 20a-c, which is the 2D illustration of Fig 17b-d respectively. Distortion angle for a particular laser scanning speed was calculated for three tracks and average value was taken. Figure 21 shows correlation between distortion angle and laser scanning speed. A positive correlation was observed between them. Since higher distortion angle represents lower amount of distortion, it can be stated that distortion

was higher at lower scanning speed. As the atoms experienced higher amount of thermal stress at lower scanning speed (Fig 19), the ribbon became prone to distortion. From heat flow analysis, it was revealed that change in free volume and resulting relaxation was higher at lower laser scanning speed. So, it appeared that relaxation induced by laser irradiation was also accompanied by structural distortion and these could be controlled by changing laser scanning speed, while keeping other parameters constant.

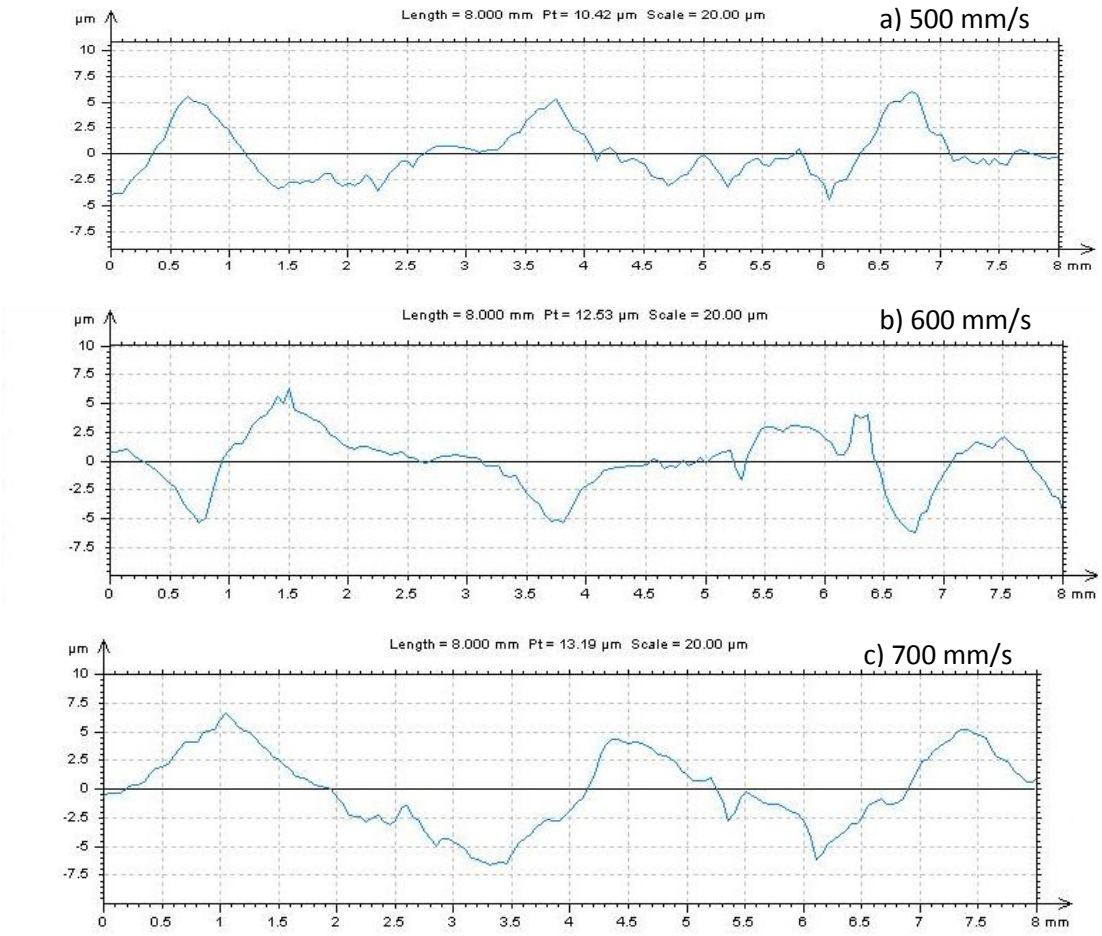

Figure 20: Distortion angle measurement for different scanning speed.

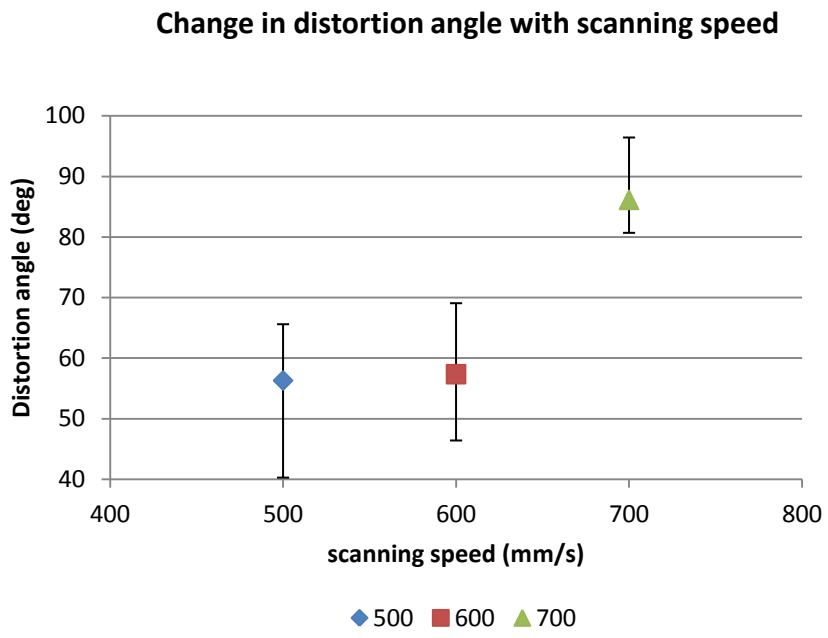

Figure 21: Variation in distortion angle with scanning speed.

Figure 22 shows heating and cooling rate during laser irradiation with different scanning speeds. Rapid heating and cooling rate for all the cases were observed in the range of 10^5 °C/s, which is a characteristic of laser irradiation. This rapid cooling inhibited atomic mobility and prevented diffusion, which was essential for amorphous phase retention (Fig 7). Heating and cooling rate was observed higher at lower laser scanning speed due to smaller interaction time. At lower irradiation time, atom would experience lesser amount of heat, so corresponding change in free volume was minimum (already discussed in heat flow analysis). Since relaxation is associated with change in free volume, it was enhanced at lower heating rate due to higher irradiation or relaxation time.

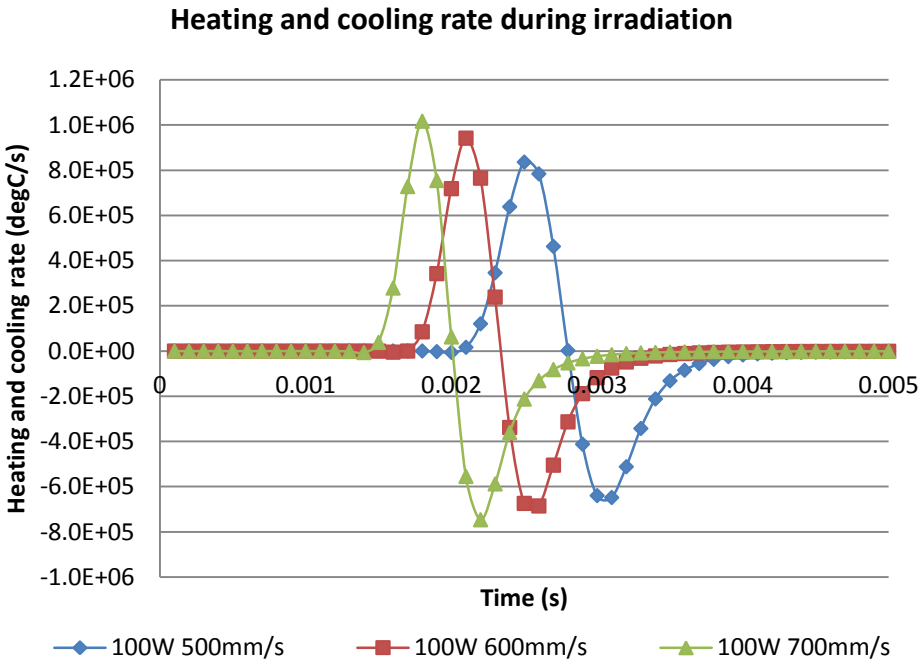

Figure 22: Heating and cooling rate variation with scanning speed.

CHAPTER 6

CONCLUSION

$Fe_{85-95}Si_{5-10}B_{1-5}$ amorphous ribbon was irradiated with continuous wave laser with three different scanning speeds, keeping other process parameters constant. Structural relaxation was analyzed and it's correlation with laser scanning speed was evaluated. Tensile strength, microhardness and surface deformation were also measured and their relation with laser scanning speed was investigated. A thermal model was developed in order to assist these observations. Based on the findings, following conclusions can be drawn:

- No clear sign of crystal formation was obtained from XRD pattern and SEM image analyses. This was further supported by thermal simulation, where temperature rise during laser irradiation was found below crystallization point.
- Laser irradiation caused significant thermal embrittlement. Reduction in fracture stress and strain for the sample irradiated with 500 mm/s laser scanning speed was more than 50%, comparing with as-received sample. This embrittlement was associated with atomic short range ordering, enhanced at lower scanning speed with greater atomic mobility.

- DSC result revealed structural relaxation by showing change in crystallization enthalpy with laser scanning speed. Reduction in enthalpy was 12% for 500 mm/s and increased with laser scanning speed. Change in enthalpy was associated with free volume change during crystallization, affected by laser heating. The increasing nature of reduction in crystallization enthalpy with laser scanning speed indicated that higher change in free volume occurred at low scanning speed during irradiation.
- Similarity in microhardness between as-received and laser irradiated ribbons was mainly due to similarity in magnetic field orientation between them. However, microhardness for 500 mm/s was found 5% higher than as-received state, possibly because of change in free volume revealed in heat flow analysis.
- Higher heating/cooling rate and surface distortion were the two consequences of site-specific heating by laser. Amount of distortion was found positively related with temperature. Change in free volume was enhanced at lower heating rate because of increase in relaxation time.

References

1. Telford, M., *The case for bulk metallic glass.* Materials today, 2004. **7**(3): p. 36-43.
2. Ma, M.Z., et al., *Wear resistance of Zr-based bulk metallic glass applied in bearing rollers.* Materials Science and Engineering: A, 2004. **386**(1–2): p. 326-330.
3. Morrison, M.L., et al., *Cyclic-anodic-polarization studies of a Zr41.2Ti13.8Ni10Cu12.5Be22.5 bulk metallic glass.* Intermetallics, 2004. **12**(10–11): p. 1177-1181.
4. Peter, W.H., et al., *Localized corrosion behavior of a zirconium-based bulk metallic glass relative to its crystalline state.* Intermetallics, 2002. **10**(11–12): p. 1157-1162.
5. Flemings, M.C., *Solidification processing.* Metallurgical Transactions, 1974. **5**(10): p. 2121-2134.
6. Inoue, A., B. Shen, and N. Nishiyama, *Bulk Metallic Glasses, eds M. Miller and P. Liaw*. 2007, Springer, New York.
7. Singh, A. and S.P. Harimkar, *Spark plasma sintering of in situ and ex situ iron-based amorphous matrix composites.* Journal of Alloys and Compounds, 2010. **497**(1–2): p. 121-126.
8. Inoue, A., *Bulk amorphous and nanocrystalline alloys with high functional properties.* Materials Science and Engineering: A, 2001. **304**: p. 1-10.
9. Johnson, W., *Bulk amorphous metal—An emerging engineering material.* Jom, 2002. **54**(3): p. 40-43.
10. Schroers, J. and W.L. Johnson, *Ductile bulk metallic glass.* Physical Review Letters, 2004. **93**(25): p. 255506.
11. Schuh, C.A., T.C. Hufnagel, and U. Ramamurty, *Mechanical behavior of amorphous alloys.* Acta Materialia, 2007. **55**(12): p. 4067-4109.
12. Demetriou, M.D., et al., *Amorphous metals for hard-tissue prosthesis.* JOM, 2010. **62**(2): p. 83-91.
13. Schroers, J., et al., *Precious bulk metallic glasses for jewelry applications.* Materials Science and Engineering: A, 2007. **449**: p. 235-238.
14. Lu, Z.P. and C.T. Liu, *A new glass-forming ability criterion for bulk metallic glasses.* Acta Materialia, 2002. **50**(13): p. 3501-3512.
15. Inoue, A. and A. Takeuchi, *High strength bulk amorphous alloys.* Mater. Trans. JIM, 2002. **43**(8): p. 1892-1906.
16. Inoue, A., B. Shen, and C. Chang, *Fe-and Co-based bulk glassy alloys with ultrahigh strength of over 4000MPa.* Intermetallics, 2006. **14**(8): p. 936-944.
17. Duwez, P., R. Willens, and W. Klement, *Continuous Series of Metastable Solid Solutions in Silver-Copper Alloys.* Journal of Applied Physics, 1960. **31**(6): p. 1136-1137.
18. Inoue, A., A. Makino, and T. Mizushima, *Ferromagnetic bulk glassy alloys.* Journal of Magnetism and Magnetic Materials, 2000. **215**: p. 246-252.
19. Hrubý, A., *Evaluation of glass-forming tendency by means of DTA.* Czechoslovak Journal of Physics B, 1972. **22**(11): p. 1187-1193.

20. Griner, S., R. Babilas, and R. Nowosielski, *Structure and properties changes of Fe78Si9B13 metallic glass by lowtemperature thermal activation process.* Journal of Achievements in Materials and Manufacturing Engineering, 2012. **50**(1): p. 18-25.
21. Babilas, R. and R. Nowosielski, *Iron-based bulk amorphous alloys.* Archives of Materials Science and Engineering, 2010. **44**(1): p. 5-27.
22. van den Beukel, A., *Analysis of chemical short range ordering in amorphous Fe40Ni40B20.* Journal of Non-Crystalline Solids, 1986. **83**(1–2): p. 134-140.
23. Tiwari, G., et al., *Structural relaxation in metallic glasses.* Materials Science and Engineering: A, 2001. **304**: p. 499-504.
24. Hammond, V.H., M.D. Houtz, and J.M. O'Reilly, *Structural relaxation in a bulk metallic glass.* Journal of non-crystalline solids, 2003. **325**(1): p. 179-186.
25. Egami, T., *Structural relaxation in amorphous alloys-compositional short range ordering.* Materials Research Bulletin, 1978. **13**(6): p. 557-562.
26. Williams, R. and T. Egami, *Effects of deformation and annealing on magnetic amorphous alloys.* Magnetics, IEEE Transactions on, 1976. **12**(6): p. 927-929.
27. Zhang, Y., W. Wang, and A. Greer, *Making metallic glasses plastic by control of residual stress.* Nature materials, 2006. **5**(11): p. 857-860.
28. Bei, H., S. Xie, and E.P. George, *Softening caused by profuse shear banding in a bulk metallic glass.* Physical review letters, 2006. **96**(10): p. 105503.
29. Cabral-Prieto, A., et al., *Spectroscopic and Mechanical Studies on the Fe-based Amorphous Alloy 2605SA1.* Journal of the Mexican Chemical Society, 2010. **54**(1): p. 7-17.
30. Escobar, M.-A., et al., *On the optimization of soft-magnetic properties of metallic glasses by dynamic current annealing.* Magnetics, IEEE Transactions on, 1992. **28**(4): p. 1911-1916.
31. Herzer, G. *Grain size dependence of coercivity and permeability in nanocrystalline ferromagnets*. in *Magnetics Conference, 1990. Digests of INTERMAG '90. International*. 1990.
32. Yoshizawa, Y., S. Oguma, and K. Yamauchi, *New Fe-based soft magnetic alloys composed of ultrafine grain structure.* Journal of Applied Physics, 1988. **64**(10): p. 6044-6046.
33. Duley, W.W., *Laser processing and analysis of materials.* New York, Plenum Press, 1983, 476 p., 1983. **1**.
34. Ion, J., *Laser processing of engineering materials: principles, procedure and industrial application*. 2005: Butterworth-Heinemann.
35. Dausinger, F., F. Lichtner, and H. Lubatschowski, *Femtosecond technology for technical and medical applications*. Vol. 96. 2004: Springer.
36. Wolbarsht, M.L., *Laser applications in medicine and biology*. Vol. 5. 1991: Plenum Publishing Corporation.
37. Steen, W.M. and J. Mazumder, *Laser material processing*. 2010: Springer.
38. Meunier, M., A. Piqueī, and K. Sugioka, *Laser precision microfabrication*. Vol. 135. 2010: Springer.
39. Dahotre, N.B. and S.P. Harimkar, *Laser fabrication and machining of materials*. 2008: Springer.
40. Bäuerle, D., *Laser processing and chemistry*. Vol. 3. 2000: Springer Berlin.
41. Basu, A., et al., *Laser surface coating of Fe–Cr–Mo–Y–B–C bulk metallic glass composition on AISI 4140 steel.* Surface and Coatings Technology, 2008. **202**(12): p. 2623-2631.

42. Sinke, W., et al., *Transient structural relaxation of amorphous silicon.* Journal of non-crystalline solids, 1988. **99**(2): p. 308-323.
43. Lanotte, L., *Tensile stress effect on magnetic properties of cw-laser annealed amorphous Fe40Ni40P14B6 ribbons.* Journal de Physique Lettres, 1983. **44**(13): p. 541-546.
44. Mudry, S. and Y. Nykyruy, *Structural changes and mechanical properties of amorphous metallic ribbons Fe–(Ni, Co, Mn)–Mo–Si–B irradiated by powerful nanosecond laser pulses.* 2011.
45. Harimkar, S.P., et al., *Periodically Laser Patterned Fe□ B□ Si Amorphous Ribbons: Phase Evolution and Mechanical Behavior.* Advanced Engineering Materials, 2011. **13**(10): p. 955-960.
46. Katakam, S., et al., *Laser-induced thermal and spatial nanocrystallization of amorphous Fe–Si–B alloy.* Scripta Materialia, 2012. **66**(8): p. 538-541.
47. Katakam, S., et al., *Stress-induced selective nano-crystallization in laser-processed amorphous Fe–Si–B alloys.* Philosophical Magazine Letters, 2012. **92**(11): p. 617-624.
48. Vora, H.D., et al., *Evolution of surface topography in one-dimensional laser machining of structural alumina.* Journal of the European Ceramic Society, 2012.
49. ; Available from: http://metglas.com/assets/pdf/2605sa1.pdf
50. Singh, A., et al., *Nanocrystallization in spark plasma sintered Fe 48 Cr 15 Mo 14 Y 2 C 15 B 6 bulk amorphous alloy.* Journal of Applied Physics, 2013. **114**(5): p. 054903-054903-7.
51. Li, X., K. Zhang, and G. Wang, *Nanoscale morphology in tensile fracture of a brittle amorphous ribbon.* Journal of materials science & technology, 2008. **24**(5): p. 745.
52. ZHANG, K.-f. and X.-f. LI, *New fracture morphology of amorphous Fe< sub> 78</sub> Si< sub> 9</sub> B< sub> 13</sub> alloy.* Transactions of Nonferrous Metals Society of China, 2008. **18**(2): p. 383-387.
53. Xi, X., et al., *Fracture of brittle metallic glasses: Brittleness or plasticity.* Physical review letters, 2005. **94**(12): p. 125510.
54. Tuinstra, P., et al., *The calorimetric glass transition of amorphous Pd< sub> 40</sub> Ni< sub> 40</sub> P< sub> 20</sub>.* Acta metallurgica et materialia, 1995. **43**(7): p. 2815-2823.
55. Mei, J., J.-L. Soubeyroux, and J.-J. Blandin. *Structural relaxation of Ti-based bulk metallic glasses*. in *PROCEEDINGS*. 2012.
56. Raghavan, R., P. Murali, and U. Ramamurty, *Influence of cooling rate on the enthalpy relaxation and fragility of a metallic glass.* Metallurgical and Materials Transactions A, 2008. **39**(7): p. 1573-1577.
57. Slipenyuk, A. and J. Eckert, *Correlation between enthalpy change and free volume reduction during structural relaxation of Zr< sub> 55</sub> Cu< sub> 30</sub> Al< sub> 10</sub> Ni< sub> 5</sub> metallic glass.* Scripta materialia, 2004. **50**(1): p. 39-44.
58. Balla, V.K. and A. Bandyopadhyay, *Laser processing of Fe-based bulk amorphous alloy.* Surface and Coatings Technology, 2010. **205**(7): p. 2661-2667.
59. Dos Santos, D. and D. Dos Santos, *Crystallization kinetics of Fe–B–Si metallic glasses.* Journal of non-crystalline solids, 2002. **304**(1): p. 56-63.
60. Avrami, M., *Kinetics of phase change. I General theory.* The Journal of Chemical Physics, 1939. **7**: p. 1103.
61. Avrami, M., *Kinetics of phase change. II transformation-time relations for random distribution of nuclei.* The Journal of Chemical Physics, 1940. **8**: p. 212.
62. Avrami, M., *Kinetics of phase change. III. Granulation, phase change, and microstructure.* J. Chem. Phys, 1941. **9**(2): p. 177-184.

63. Liu, X., et al., *Observation of the crystallization of amorphous Fe・Cu・Si・B alloy by< i> in situ</i> transmission electron microscopy.* Materials Science and Engineering: A, 1994. **179**: p. 386-389.
64. Mehta, N., K. Singh, and N. Saxena, *Co-relation between pre-exponential factor and activation energy of non-isothermal crystallization for virgin and irradiated Fe< sub> 78</sub> B< sub> 13</sub> Si< sub> 9</sub> metallic glass.* Physica B: Condensed Matter, 2009. **404**(16): p. 2184-2188.
65. Piller, J. and P. Haasen, *Atom probe field ion microscopy of a FeNiB glass.* Acta Metallurgica, 1982. **30**(1): p. 1-8.
66. Gerling, R., F. Schimansky, and R. Wagner, *Two-stage embrittlement of amorphous Fe< sub> 40</sub> Ni< sub> 40</sub> P< sub> 20</sub> resulting from a loss of free volume and phase separation.* Acta Metallurgica, 1988. **36**(3): p. 575-583.
67. Chen, H., *Thermal and mechanical stability of metallic glass ferromagnets.* Scripta Metallurgica, 1977. **11**(5): p. 367-370.
68. Wu, T. and F. Spaepen, *Small angle X-ray scattering from an embrittling metallic glass.* Acta Metallurgica, 1985. **33**(12): p. 2185-2190.
69. Fish, G. and H. Child, *Studies of chemical homogeneity and magnetic domain walls in Fe-based metallic glasses using small-angle neutron scattering.* Journal of Applied Physics, 1981. **52**(3): p. 1880-1882.
70. Kumar, G., et al., *Thermal embrittlement of Fe-based amorphous ribbons.* Journal of Non-Crystalline Solids, 2008. **354**(10): p. 882-888.
71. Yavari, A., et al., *Rapid annealing of Fe-Si-B amorphous tapes by joule heating: Effects on magnetic and mechanical properties.* Journal of magnetism and magnetic materials, 1987. **69**(1): p. 43-52.
72. Yovanovich, M. *Micro and macro hardness measurements, correlations, and contact models*. in *Collection of technical papers—44th AIAA aerospace sciences meeting*. 2006.
73. Vollertsen, F., I. Komel, and R. Kals, *The laser bending of steel foils for microparts by the buckling mechanism-a model.* Modelling and Simulation in Materials Science and Engineering, 1995. **3**(1): p. 107.

VITA

Md Farhadul Haque

Candidate for the Degree of

Master of Science

Thesis: EFFECT OF CONTINUOUS WAVE LASER IRRADIATION ON STRUCTURAL RELAXATION AND MECHANICAL PROPERTIES OF Fe-Si-B AMORPHOUS RIBBON

Major Field: Mechanical and Aerospace Engineering

Biographical:

Education:

Completed the requirements for the Master of Science in Mechanical and Aerospace Engineering at Oklahoma State University, Stillwater, Oklahoma in December, 2013.

Completed the requirements for the Bachelor of Science in Mechanical Engineering at Bangladesh University of Engineering and Technology, Dhaka, Bangladesh in 2009.

Experience:

- 2 years and 4 months of experience as Graduate Teaching Assistant in Oklahoma State University, Stillwater, Oklahoma
- 2 years of experience as Sales Engineer in compressor technique in Atlas Copco Bangladesh Limited, Dhaka, Bangladesh
- 2 months of experience as Service Engineer in diesel engine generator in Mir Trading Company, Dhaka, Bangladesh
- Authored 1 conference paper in 13 Asian Congress of Fluid Mechanics, Dhaka, Bangladesh